UCRL-JRNL-228005

LAWRENCE
LIVERMORE
NATIONAL
LABORATORY

Ground motion modeling of the 1906 San Francisco earthquake II: Ground motion estimates for the 1906 earthquake and scenario events

B. Aagaard, T. Brocher, D. Dreger, A. Frankel, R. Graves, S. Harmsen, S. Hartzell, S. Larsen, K. McCandless, S. Nilsson, N. A. Petersson, A. Rodgers, B. Sjogreen, H. Tkalcic, M. L. Zoback

February 13, 2007

Bulletin of the Seismological Society of America

Disclaimer

This document was prepared as an account of work sponsored by an agency of the United States Government. Neither the United States Government nor the University of California nor any of their employees, makes any warranty, express or implied, or assumes any legal liability or responsibility for the accuracy, completeness, or usefulness of any information, apparatus, product, or process disclosed, or represents that its use would not infringe privately owned rights. Reference herein to any specific commercial product, process, or service by trade name, trademark, manufacturer, or otherwise, does not necessarily constitute or imply its endorsement, recommendation, or favoring by the United States Government or the University of California. The views and opinions of authors expressed herein do not necessarily state or reflect those of the United States Government or the University of California, and shall not be used for advertising or product endorsement purposes.

Ground Motion Modeling of the 1906 San Francisco Earthquake II: Ground Motion Estimates for the 1906 Earthquake and Scenario Events

by Brad T. Aagaard, Thomas M. Brocher, Douglas Dreger, Arthur Frankel, Robert W. Graves, Stephen Harmsen, Stephen Hartzell, Shawn Larsen, Kathleen McCandless, Stefan Nilsson, N. Anders Petersson, Arthur Rodgers, Björn Sjögreen, Hrvoje Tkalcic, and Mary Lou Zoback

January 31, 2007

For submission to BSSA

Abstract [ADD ABSTRACT HERE]

Introduction

[ZOBACK]

The 18 April 1906 magnitude 7.9 San Francisco earthquake ruptured the San Andreas fault for nearly 500 km with a mean slip of about 4 m (Song *et al*., 2008). The occurrence and subsequent investigation of this earthquake (Lawson and Reid, 1908) [MARY LOU: IS THE CITATION INFO CORRECT?] marked the birth of modern earthquake science in the United States. For the first time a large earthquake and its effects were systematically documented and the shaking was properly interpreted as resulting from slip on an active fault and as part of a recurring geologic process. To commemorate the centennial of the 1906 earthquake, a two-year collaborative effort was launched to recreate the strong ground motion produced by this event. By utilizing modern computational methods and taking advantage of new data and constraints we are able to characterize both the amplitude and duration of shaking in 1906 across northern California. Aagaard *et al*. (2008) discusses our efforts to validate the 3-D geologic and seismic velocities models used in this study with data from the 1989 Loma Prieta earthquake.

The 1906 earthquake was felt throughout California, in southern Oregon, and as far east as central Nevada. It also wrote the first useful strong motion record, a three-component pendulum recording at Mount Hamilton, about 90 km from the epicenter. More than 600 detailed reports of shaking intensity and damage were compiled in the two-volume landmark document, *The Report of the State Earthquake Investigation Commission*, edited by Lawson and Reid (1908). Based on these data, the Commission investigators concluded that, in general, shaking intensity diminished with distance from the fault. They also recognized the importance of site effects, noting that the "amount of damage produced by the earthquake . . . depended chiefly on the geological character of the ground" (H. O. Wood), and, in particular, commented that "areas that suffered most severely were those upon filled ground". To help explore the phenomena that shaking intensity was stronger on soft ground than on rock at comparable distances from the fault, graduate student H. G. Rogers (volume I, pages 326–335) designed an ingenious set of experiments measuring the amplitude of shaking of sand in a vibrating box. He found that dry sand moved simply with the box, whereas the amplitude of shaking in wet sand depended both on the degree of saturation and frequency of the imposed vibrations. While cognizant of possible shortcomings related to the scale and possible influence of edge effects in such experiments, Rogers concluded that at seismic frequencies the amplitude of motion of soft, water-filled sediments is greater than that in the surrounding rock. Commission member H. F. Reid applied mathematical theory to extend the application of these vibrating sand box experiments. He properly concluded that the response of basins depended on their size relative to the wavelength of the seismic waves, and that in large basins internal reflections could result in increased amplification (volume II, page 54), and that variations in amplitude within and between large basins were related to "differences in the character and depth of the alluvium" (volume II, page 56). Our ground motion modeling results demonstrate all of these effects, indicating the robustness of these early observations, modeling and interpretations.

Previous investigations of the 1906 earthquake have used Lawson and Reid (1908) to constrain the location, source, and ground motions for the event. Boore (1977) interpreted phases in the sole strong motion recording at Mt. Hamilton to constrain the epicentral location to lie somewhere offshore from San Francisco and likely much further south than the previously presumed epicenter near Olema (which had been based on its association with large surface displacements (Lawson and Reid, 1908)[VOLUME II, REID 1910??]). More recently Lomax (2005) reevaluated the arrival-time observations and applied modern event-location techniques to determine a maximum-likelihood hypocenter of 37.78° N, 122.51° W at a depth of about 12 km. Wald *et al*. (1993) combined the preserved teleseismic records with emprirical Green's functions to construct a finite source model for the 1906 earthquake; however, the slip distribution differs markedly from the one Thatcher *et al*. (1997) developed based on triangulation surveys. A new source model (Song *et al*., 2008) that combines both datasets appears to resolve many of the discrepancies between the two.

Borcherdt and Gibbs (1976) combined modern site response data with intensity mapping in Lawson and Reid (1908) to estimate the variability in response for various geologic units and quantify the dependencies of the 1906

shaking intensities with distance from the rupture and site conditions. Anooshehpoor *et al*. (1999) calculated a lower-bound for the peak acceleration of about 1 g at frequencies less than 2 Hz at the Point Reyes train station based, in part, on the conductor's description of the ground motions that overturned the train as documented in Lawson and Reid (1908). Ward (2000) created a quasi-static model of the 1906 earthquake with modified whole-space Green's functions and using the geodetic slip model from Thatcher *et al*. (1997) computed a very rough estimate of the variability of shaking. The simulated ground motions were limited to a few stations and included directivity, but not 2-D or 3-D Earth structure. As a result, these simulations fail to capture the dynamics (i.e., rise time) of the source.

Boatwright and Bundock (2005) constructed a ShakeMap for the 1906 earthquake (Figure 1) by carefully examing all of the shaking and damage reports compiled in Lawson and Reid (1908) and reinterpreting them in terms of the modern modified Mercalli Intensity scale. This ShakeMap provides a much more comprehensive picture of the shaking intensities and serves as the primary independent constraint in our ground motion simulations. Shaking intensities, such as those in ShakeMap, however, lack information about the duration and character of the ground motion. Our ground motion simulations utilize up-to-date information on the 3-D crustal structure and our experience in generating realistic kinematic source models to produce ground motion time histories over the San Francisco Bay area and the surrounding region extending more than 500 km along the San Andreas fault. We also investigate the variability in ground motions for similarly sized events on this portion of the San Andreas fault due to changes in the hypocenter (and rupture directivity) and differences in the distribution of slip.

Methodology

For our ground motion modeling of the 1906 earthquake we use the Song *et al*. (2008) source model, which constrains the slip distribution using both telseismic records and triangulation surveys and and the rupture speed using the teleseismic records. Even with these combined datasets many important details and source parameters are missing from the rupture model. We filled in the missing details, such as short-length scale variations in slip and rise time, based on empirical observations and parameter searches, in which we attempted to fit Boatwright and Bundock's shaking intensities. Given the large uncertainty in the source parameters, we worked in parallel in five ground motion modeling groups to search the parameter space and constrain the missing details, yielding our "preferred" source model for generating strong ground motions from the 1906 earthquake.

Numerical Models

[AAGAARD]

The five ground motion modeling groups included Aagaard, Graves, Harmsen *et al.* (Harmsen, Hartzell, and Frankel), Larsen *et al.* (Larsen and Dreger[1]), and Petersson *et al.* (Petersson, Rogers, McCandless, Nilsson, Sjögreen, and Tkalcic). Each group used a different modeling code to solve the elastic wave equation. Four of these codes were used in our efforts to model the Loma Prieta earthquake (Aagaard *et al*., 2008). The other one, called WPP (Wave Propagation Project), used by Petersson *et al.* and developed by Nilsson *et al*. (2006) employs node-centered (non-staggered) finite-differences with a displacement formulation to discretize the elastic wave equation.

Table 1 gives the sizes and various features of the numerical models. Many of the features and parameters match those used in modeling the Loma Prieta earthquake. Some notable exceptions include the bounding boxes for the Graves and Larsen *et al.* modeling groups and the inclusion of topgraphy and attenuation in the Larsen *et al.* simulations. Simulating wave propagation through the 3-D structure in the volume surrounding the entire rupture length of the 1906 earthquake at periods of 1–2 seconds and longer requires extensive computational resources. As a result, Aagaard and Harmsen *et al.* model only portions of the rupture, whereas the domains for Graves, Larsen *et al.*, and Petersson *et al.* cover the entire rupture as shown in Figure 2.

Another difference with respect to the Loma Prieta simulations is that in this study the Graves, Larsen *et al.*, and Petersson *et al.* domains extend well beyond the boundaries of the detailed portion of the velocity model and into the coarser resolution regional portion as shown in Figure 2. While there is a smooth transition from the detailed portion to the regional portion, the regional portion contains only a few major geologic units. As a result, we expect to capture much less detail in the spatial distribution of shaking and the waveforms in the areas of the numerical models that lie in the regional portion of the velocity model.

All of the numerical models use the fault geometry of the San Andreas fault from the 3-D geologic model. For the four finite-difference numerical models, in which the earthquake rupture is implemented with point sources, we discretize the fault surface into a 1 km uniform resolution logically rectangular grid that conforms to the nonplanar geometry of the continuous surface. Aagaard's numerical model incorporates the fine resolution triangulated surface as an interior interface in the numerical model, with the same smoothing as was used in the Loma Prieta modeling.

[ADD: INFO ON WHAT PROJECTIONS WERE USED OR WHAT PROJECTIONS BEST CORRESPOND TO THE MAPPINGS USED FOR GRAVES, HARMSEN ETAL, LARSEN ETAL, PETERSSON ETAL]

Including Short-Period Energy

[GRAVES]

[1]Note that in this study we refer to the Larsen and Dreger group as Larsen *et al.* whereas in the Loma Prieta study we referred to the Dolenc, Dreger, and Larsen group as Dolenc *et al.*.

Graves extended his simulations to shorter periods using the same hybrid procedure as he did for the Loma Prieta simulations. The hybrid procedure generates broadband ground motions, in this case T $<$ 0.1 s, by combining stochastic modeling at short-periods (T $<$ 1 s) with the deterministic modeling (described in the previous section) at long periods (T $>$ 1 s). The modeling technique also applies site corrections across all periods to account for near-surface site effects.

[ADD: NOTE 1-D VELOCITY MODEL IS SAME AS IN LOMA PRIETA SIMULATIONS]

Source Models

[GRAVES]

In addition to adapting the Song *et al.* source model for use in our strong ground motion simulations, we also constructed source models for seven hypothetical scenarios in order to characterize the potential variability in ground motions for events of this size on the northern San Andreas fault. Table 2 gives the label of each of the scenarios along with the names of the corresponding slip models and hypocenters. Three of these are simply perturbations from our adapted Song *et al.* model with different hypocenters. The other four scenarios use distributions of slip and rupture speed that are significantly different from that in the Song *et al.* source model but use the 1906 hypocenter and the same three hypothetical hypocenters.

Slip Time Function

[AAGAARD]

In each of the source models, we employ the same slip time function that we used in our Loma Prieta simulations Aagaard *et al*. (2008). The slip time history follows the integral of Brune's far-field time function,

$$D(t) = D_{final}(1 - e^{-t/t_0})(1 + \frac{t}{t_0}), \tag{1}$$

$$t_0 = \frac{D_{final}}{eV_{max}}, \tag{2}$$

$$V_{max}[m/s] = C_{tr}\sqrt{D_{final}[m]}, \tag{3}$$

$$C_{tr} = \begin{cases} 0.6 & z \geq 0 \text{ km} \\ -0.12z + 0.6 & -5.0 \text{ km} < z < 0 \text{ km} \\ 1.2 & z \leq -5.0 \text{ km} \end{cases} \tag{4}$$

where $D(t)$ is the slip as a function of time, D_{final} is the final slip at a point, V_{max} is the peak slip rate, and z is the elevation with respect to sea level. The primary feature of this slip time function is that the rise time (the time it takes

for 95% of the slip to occur, t_{95}), which is given by

$$t_{95} = 1.745\frac{D_{final}}{V_{max}}, \text{ where} \tag{5}$$

$$D(t_{95}) = 0.95D_{final}, \tag{6}$$

is in the range of 3–4 seconds for slip in the range of 4–8 meters when $C_{tr} = 1.2$. This is consistent with the average rise time expected for events of this size (Somerville *et al.*, 1999). We lengthen the rise time near the surface based on preliminary simulations with the Song2 model in which longer rise times in the near-surface region improved the fit to the Boatwright and Bundock intensities, and emprical observations of longer rise times for large surface rupture (Kagawa *et al.*, 2004).

Adapting the Song *et al.* Model

[GRAVES]

The Song *et al.* model uses a hypocenter consistent with the geometry of the San Andreas fault in the 3-D geologic model and the Lomax probability analysis. This yields a location of 122.55° W, 37.75° N, and a depth of 10 km. As mentioned earlier, the Song *et al.* source model only contains slip variations at long length-scales and a rather rough estimate of the rupture speed. The source model specifies slip on 10 km along-strike and 12 km down-dip patches, with the average rupture velocity determined over portions ranging in length from 40 km to 120 km. The inversion could resolve neither the slip time function nor slip rise time. In order to accurately estimate the ground motions in the period range of interest (about 1 to 2 seconds and longer), our ground motion simulations require a finer scale resolution of the rupture properties, which necessitated incorporating additional information and making several small adjustments.

First, we taper the rupture velocity in the upper 5 km of the fault to be 60% of the original Song *et al.* value. This modification follows from both variations in rupture speed associated with slower shear wave speeds in the top few kilometers of the crust and relatively slower ruptures speeds in near-surface regions for large events with surface rupture (e.g., Somerville *et al.* (1999)). Figure 3 shows the distributions of slip with contours of slip initiation time for this source model (hereafter referred to as Song2).

As we will discuss later, preliminary analyses with the Song2 model indicated that reducing the slip by 30% (corresponding to a reduction in magnitude from 7.9 to 7.8) substantially improved the fit to the Boatwright and Bundock intensities. This led us to construct a set of source models with an average slip 30% less than that in the Song2 model. Additionally, in these models we added randomly phased, shorter length scale slip variations that have a wavenumber squared falloff consistent with studies of kinematic source inversions (Somerville *et al.*, 1999; Mai and

Beroza, 2002). The form of the wavenumber filter applied to the slip distribution is given by

$$A(k) = C(1+k_0^4)^{-1/2}, \tag{7}$$

$$k_0^2 = k_x^2 x_L^2 + k_y^2 y_L^2 \tag{8}$$

where k_0 is the normalized wavenumber, C is a scaling factor to give the corrent seismic moment, and x_L and y_L are correlation lengths given by

$$\log_{10} x_L = \log_{10} y_L = 0.5M_w - 2. \tag{9}$$

In order to preserve the long wavelength features of the original model, no filtering is applied to wavelengths greater than 20 km.

We also incorporated local variations in rupture speed based on observations that ruptures tend to propgate faster in regions with larger slip as seen in spontaneous rupture models (e.g., Day (1982)) and inferred from source inversions of past earthquakes (Hisada, 2001). We adjust the slip initiation times according to

$$t_r = t_{orig} - t_{shift}(slip), \tag{10}$$

where t_r is the slip initiation time, t_{orig} is the slip initiation time given by the Song2 model, and $t_{shift}(slip)$ is a timing perturbation that scales linearly with slip amplitude such that $t_{shift} = 1.0$ s at the location of maximum slip and $t_{shift} = 0$ at locations where the slip is equal to the average value. Applying the above modifications to the Song2 rupture model yields a source model we refer to as Song2b. Our final 1906 rupture model (Song2c) further modifies the Song2b model with some slight adjustments in an attempt to improve the fit to the Boatwright and Bundock intensities. The adjustments include perturbing the distribution of slip at long wavelengths in the Bodega Bay area (30–100 km north of the epicenter) and a few stretches between San Francisco and San Jose, and reducing the rupture speed in the southern most 40 km of rupture. Figure 3 contains the Song2c model in the middle panel. The electronic supplement contains the detailed specifications for each of the source models.

Scenario Source Models

[GRAVES]

The first set of scenario rupture models use the same distributions of slip and rupture speed as the Song2c source model; however, we consider three alternative hypocenter locations: one near the northern end of the rupture (Rockport), one near the center of the rupture (Bodega Bay), and one near the southern end of the rupture (San Juan Bautista). We refer to these scenarios as Scenario2cHypoN, Scenario2cHypoC, and Scenario2cHypoS, respectively. Table 3 gives the precise hypocenters and Figure 4 provides a map of the locations.

We also consider a set of purely hypothetical rupture models making use of the same rupture geometry. We generate a slip distribution with random phase at all wavelengths using the wavenumber squared filter given in equation (7) while constraining the average slip to be the same as the Song2c source model. We generated several realizations of the slip model and chose one whose spatial distribution differed substantially from that in the Song2c source model. The slip initiation time follows equation (10), where $t_{orig} = d/v_r$ and d denotes the rupture path length from the hypocenter and v_r denotes the rupture speed. In these scenarios we prescribe an average rupture speed of 80% of the local shear wave speed. We construct source models with these parameters for the 1906 hypocenter as well as the three hypothetical hypocenters. We refer to these scenarios as ScenarioR04Hypo06 (R04 refers to the random realization), ScenarioR04HypoN, ScenarioR04HypoC, and ScenearioR04HypoS. Figure 3 includes the slip distribution for ScenarioR04HypoN.

Results

We now focus on the results of the simulations, first considering the 1906 earthquake and then the scenario events. We examine the consistency of the results across the five numerical models and how well the shaking intensities from the simulations of the 1906 earthquake agree with those in the ShakeMap constructed by Boatwright and Bundock (2005).

1906 Earthquake

[RODGERS]

The Modified Mercalli Intensity (MMI) values for the 1906 earthquake reported by Boatwright and Bundock, shown in Figure 1, indicate that the strongest shaking was experienced along the San Andreas fault. In fact most locations within 50 km of the rupture length experienced shaking intensities of MMI seven or greater. Two regions suffered particularly high shaking, the area extending from Tomales Bay to Santa Rosa (see Figure 4 for placename locations) and the southern Santa Cruz Mountains southwest of San Jose. High intensities were also experienced along the northern California coast, with MMI values greater than eight south of Point Arena and at Cape Mendocino.

These regions with particularly intense shaking north of San Francisco correlate well with large slip (more than 4 m) along the fault directly north of the epicenter. The strong shaking from Tomales Bay to Santa Rosa appears to be accentuated by directivity effects and the super-shear rupture speed (>4.5 km/s) in the first 100 km of rupture north of the epicenter. Strong shaking in Santa Rosa was likely exacerbated by low-velocity basin fill (McPhee *et al.*, 2008).

Fit to Inferred Shaking Intensities

[RODGERS]

Figures 5 and 6 display synthetic ShakeMaps for the Aagaard and Larsen *et al.* SF1906Song2 simulations, which use the the Song2 source model. We constructed these ShakeMaps following the same procedure we used for the Loma Prieta simulations (Aagaard *et al*., 2008), wherein we compute Modified Mercalli Intensity (MMI) values from PGV values using the PGV to MMI relation developed for ShakeMap (Wald *et al*., 2005). This procedure also permits construction of the maps with pointwise differences between the synthetic intensities and the Boatwright and Bundock intensities (also shown in Figures 5 and 6). The synthetic intensities reveal a pattern of ground motion similar to the Boatwright and Bundock intensities. Ground motions are highest along the San Andreas fault, especially where the estimated slip was high, and decrease away from the fault. The simulations also capture the pattern of high intensities between Tomales Bay and Santa Rosa.

The Boatwright and Bundock intensities have the greatest density within the San Francisco Bay area. This area also coincides with the detailed portion of the velocity model, so that our simulations are generally more accurate within this area as well. The synthetic intensities for the SF1906Song2 simulation in the San Francisco Bay area, as illustrated in Figure 5, over predict the Boatwright and Bundock intensities by an average 0.89 MMI units. Note that this average misfit includes the contributions from regions offshore. The misfit is largest in the Santa Cruz mountains west of San Jose, where the synthetic intensities are at least two MMI units greater than the Boatwright and Bundock intensities over a significant area, and at the southern end of the rupture. Only a very few, scattered locations under predict the shaking intensities.

Based on our Loma Prieta simulations with a well-constrained source model, we would expect the synthetic intensities to have some scatter while under predicting the observed intensities on average. Several factors contribute to significantly greater uncertainty in calculating the misfit in the intensity values for the 1906 earthquake. In this case, instead of comparing the synthetic intensities to instrumental intensities, we compare them with the Boatwright and Bundock intensities, which are inferred from damage reports from structures built before modern building codes. This makes calibration of intensity assignments much more difficult. Furthermore, the ShakeMap relation for computing MMI from PGV is constrained using events up to magnitude 7.3 [CHECK THIS] with very little data at peak velocities exceeding 1 m/s. Thus, the relationship is not well-constrained for velocities greater than 1 m/s (MMI values of 9 and greater) or magnitude 7.8–7.9 events. This greater uncertainty in the misfit in shaking intensities suggests that we might not expect to under predict the Boatwright and Bundock shaking intensities. In fact, with larger events radiating energy at longer periods and with the Boatwright and Bundock intensities associated with damage to short-period structures, we might expect the ShakeMap PGV/MMI relationship to over predict the Boatwright and Bundock intensities.

The average misfit of 0.89 MMI units in Aagaard's SF1906Song2c simulation corresponds to an over prediction in PGV of about 80%. Even with the greater uncertainty in determining the misfit, this level of misfit implies the synthetic intensities may be too high. Small increases to the rise time (reducing the peak slip rate) produce only slight reductions in the mean misfit. In order to reduce the misfit significantly, the rise time must be increased by about a factor of two. Such rise times are significantly longer than those observed in kinematic source observations (Somerville *et al*., 1999). Reducing the slip by 30%, however, decreases the misfit by a factor of two as illustrated in Figure 5 using the SF1906Song2c simulation with the Song2c source model. This misfit of 0.43 MMI units corresponds to a misfit in PGV of only about 30%, suggesting that the SF1906Song2c simulation gives a reasonable match to the Boatwright and Bundock intensities. Later we discuss one way to construct a source model that gives a similar fit to the intensities while preserving the moment magnitude of 7.9 from the Song *et al.* source model.

Examining the misfit in shaking intensities over the entire rupture length for the Song2 source model using Figure 6, we find the synthetic intensities over predict the Boatwright and Bundock intensities over most of the region north of Santa Rosa and Sacramento. This area lies outside the detailed portion of the velocity model, so the simulations capture only the most basic geologic effects. For example, the misfit at the northern end of the Great Valley north of Sacramento can be attributed to greatly simplified geologic structure in the regional portion of the velocity model. On the other hand, the over prediction of the intensities in the region adjacent to the rupture north of Santa Rosa is associated with MMI values of 10+ and peak velocities exceeding 2 m/s. Over Larsen *et al.*'s entire simulation domain (including constributions from the regions offshore) the synthetic intensities exceed the Boatwright and Bundock intensities by an average of 1.3 MMI units. As in the San Francisco Bay area, the SF1906Song2c simulation, with reduced slip, reduces the mean misfit to 1.0 MMI units. The poor resolution of the regional velocity model, especially north of Sacramento, prevents the misfit from dropping as much as it did for the Aagaard simulations, which are confined to the detailed portion of the velocity model.

Geodetic Displacements

[LARSEN]

The geodetic displacements computed by Song *et al*. (2008) from the triangulation surveys provide another, albeit not independent, data source with which to judge the SF1906Song2 and SF1906Song2c simulation results. Note that Song *et al.* used a homogeneous half-space in modeling the triangulation surveys while the displacements in the simulations are computed using the 3-D seismic velocity model. Figure 7 shows that the static surface offsets calculated from the SF1906Song2 ground motion simulation follow the geodetically-derived surface motions corresponding to the triangulation surveys. This is expected because the slip for the Song2 rupture model was heavily constrained by the

geodetic data. In fact, the discrepancies between the simulations and the geodetic displacements correspond to the misfit in displacements for the Song2 source model (which is constrained by both geodetic and seismic observations). In other words, including 3-D material properties, nonplanar fault geometry, and topography do not significantly change the misfit from that already present in the Song2 source model.

The adjustements made to the Song2 source model in constructing the Song2c source model, i.e., reducing the slip by 30% and applying a wavenumber squared filter to the slip distribution, slightly degrades the fit to the geodetic displacements. The wavenumber filter appears to have a greater impact as the displacements at some sites very close to the fault, such as the pair of sites just south of Cape Mendocino, undergo substantially more changes than a mere 30% reduction in magnitude. A modern strong motion network provides resolution of the spatial variation of slip across a much broader range of length scales than what is present in the Song *et al.* source model, so that joint inversions with geodetic and seismic data for most recent earthquakes would naturally have the spectral characteristics we had to artificially impose. Thus, our adjustments to the Song2 source model to make it suitable for strong ground motion modeling, which we applied to overcome limitations of the data available, do degrade the fit to the geodetic displacements, but the static displacements in the simulations continue to reproduce the primary features observed in the triangulation surveys.

Consistency Across Modeling Groups

[RODGERS]

With significantly better fits to the intensities using the SF1906Song2c simulations, we now focus on the consistency in the shaking intensities and ground motions across the numerical models for this realization of the 1906 earthquake. Figures 8 and 9 display the shaking intensities for the other three modeling groups, including the extension of the Graves simulation to shorter-periods. All five of the numerical models produce similar patterns of shaking intensity (the electonic supplement contains additional figures that more directly illustrate the consistency of the shaking intensities). The intensities are greatest along the San Andreas fault with sedimentary basins accentuating high intensities at some locations, such as Santa Rosa (Windsor and Cotati basins) and southest of San Jose (Cupertino basin).

The differences in mean misfit with respect to the Boatwright and Bundock intensities result primarily from the use of different modeling domains, but differences in the numerical methods also contribute. For example, the Harmsen simulations predict a smaller bias in the intensities, but the simulation domain covers a smaller area where the synthetics best reproduce the Boatwright and Bundock intensities. The Petersson *et al.* simulation yields a similar misfit in the San Francisco Bay area but exhibits a strong trend of increasing misfit at greater distances from the

epicenter due to an absence of attenuation in the numerical model. They also report the peak magnitude of the vector horizontal velocities as opposed to the maximum peak of the horizontal components as the other groups did (this second metric matches the ShakeMap definition of PGV). The shaking distribution from Graves' long-period simulation very closely matches the one from Larsen *et al.* simulation; the Larsen *et al.* intensities are generally about 0.5 MMI units higher due to a slower minimum shear wave speed.

[ADD: COMMENTS ON GRAVES BROADBAND AND EFFECT OF ADDING SHORTER PERIODS]

Velocity Waveforms

[LARSEN]

Velocity waveforms provide significantly more infomation about the ground motions than a single intensity metric, such as MMI. For example, they include information about the duration of shaking as well as the polarity of motion. We do not have strong motion records with which to directly constrain the waveforms, but we do have indirect constraints through the source model and the Boatwright and Bundock's intensities. Hence, the velocity waveforms should be indicative of the amplitude and overall duration of shaking with more accurate motions in the detailed portion of the seismic velocity model. Table 4 and Figure 10 give the locations of six sites associated with the velocity waveforms for the SF1906Song2c simulations displayed in Figures 11–16 (see the electronic supplement for waveforms at four additional sites). All of these six sites lie within the detailed portion of the velocity model except for Eureka, which lies near the northern end of the regional portion of the model.

The velocity waveforms in San Francisco (site SF472, Figure 11) show a strong double-sided pulse in the north-south direction with a weaker pulse in the east-west direction, consistent with a strong fault-parallel pulse in the northwest-southeast direction associated with the SH wave radiated perpendicular to the fault away from the epicenter. The strong shaking begins within a few seconds of the rupture initiation and ends about 15 seconds later. The topographic boundary condition in the Larsen *et al.* numerical model appears to create some numerical noise in the velocity time histories; it is not present in the Aagaard *et al.* waveforms which include topography via natural boundary conditions. The amplitudes in the Harmsen *et al.* velocity waveforms are smaller than the others because the Harmsen *et al.* model is truncated just north of San Francisco so that the waveforms are missing contributions from the source north of the domain boundary.

Rupture directivity and local geologic structure influence the waveforms in San Jose (site SF474, Figure 12). The strong shaking does not begin until about 20 seconds after rupture initiation and lasts for about 55 seconds. Direct shear waves and Love waves eminating from the nearby Cupertino basin west of San Jose dominate the motions. Love waves arriving at about 45 seconds produce the peak velocities. The early phases are very similar across all five numerical

models. The Graves simulation predicts significantly less of a basin response than the other four simulations, which all show a strong basin response beginning at about 40 seconds.

In Livermore (site SF292, Figure 13) the local sedimentary basin amplifies the shaking, but the amplitudes are smaller than in San Jose due to the greater distance from the rupture. Relative to the epicenter, Livermore lies near a node in the shear-wave radiation pattern and a peak in the dilatational-wave and Rayleigh-wave radiation patterns. This results in a relatively weak onset to the motion at about 22 seconds with larger amplitude shaking corresponding to the Rayleigh waves dominating the motion from 30–45 seconds. The numerical models produce very similar motions at Livermore, capturing both the early phases and the Rayleigh waves.

The Cotati and Windsor basins strongly influence the waveforms in Santa Rosa (site SF501, Figure 14). Large slip north of the epicenter and the super-shear rupture speed directs energy towards Santa Rosa, which when combined with amplification in the basin, creates a very strong shear-wave arrival at about 22 seconds in the east-west direction. The complex basin structure creates a beating effect in the ground motions, especially in the north-south direction, where strong shaking at around 26–36 seconds is followed by a short lull before strong shaking returns for about 16 more seconds. Differences in the resolution of the numerical models and sampling of the geologic model associated with how the models implement topography appear to create small differences in the waveforms among the numerical models, especially for the later arrivals in the east-west direction. Nevertheless, the north-south and vertical components of the numerical models give a consistent indication that the duration of strong shaking was about 40 seconds.

Only two of the numerical models, Graves and Larsen *et al.*, provide waveforms at the site in the delta region of the Sacramento-San Joaquin rivers (site CT06013301000, Figure 15). Both simulations illustrate that shear and Love waves with periods in the range of 8–10 seconds dominate the waveforms at this site. The distance from the source coupled with slow near-surface sediments result in a relatively slow decay in motions over about 50 seconds.

Shear-wave directivy controls the ground motions in Eureka (site SF172, Figure 16). Eureka sits in the forward directivity direction so that all of the strong shear-wave energy radiated along the fault from the epicenter to the northern extent of rupture arrives in a short time-window. As a result, the motions are dominated by large-amplitude, long-period velocity pulses polarized in the east-west direction. The duration of very strong shaking is only about 20 seconds. The numerical models show excellent consistency in the waveform shape for these velocity pulses, but the Larsen *et al.* simulation predicts slightly larger amplitudes than the Graves simulation.

Earthquake Scenarios

[HARMSEN/HARTZELL]

We do not know the slip distribution or the hypocenter of future large earthquakes on the northern San Andreas fault, so we have considered alternative hypocenters with the Song2c source model, as well as a random slip distribution with the same suite of different hypocenters. Contrasting the Random04 slip distribution with the Song2c model, the San Francisco to Tomales Bay portion of the rupture has less slip, whereas the San Jose to San Francisco portion has more slip. In the random slip source models we also keep the rupture subshear over the entire rupture extent. This reduces the rupture speed in the first 100 km north of the epicenter compared with the simulations using the Song2c rupture speed distribution.

Changing the hypocenter directly affects the rupture directivity and has the strongest influence on the overall distribution of shaking for our suite of eight earthquake simulations. In each case rupture directivity generates strong shaking along the fault away from the epicentral region, creating strong correlations between the distributions of shaking for each pair of simulations with the same hypocenter (comparing Figures 5–6 and 17–19 with Figures 20–23). Most areas subjected to the strongest shaking with the Song2 distribution of slip are also subjected to the strongest shaking with the Random04 distribution of slip. These areas are generally confined to regions in close proximity to the fault rupture and regions with softer near-surface sediments, such as the southern perimeter of the San Francisco Bay, the delta of the Sacremento and San Joaquin rivers, and the Santa Rosa area. In the San Francisco Bay region, the strongest directivity and ground motions with MMI values greater than 8 arise from rupture starting at northern and central hypocenters (Rockport and Bodega Bay). Areas near the northern and southern ends of the Great Valley also tend to experience significant shaking with MMI values around 7, but these are areas within the regional seismic velocity model where our simulations are not as accurate due to the coarse resolution of the geologic structure.

The most significant changes in the distributions of shaking intensity occur along the San Francisco peninsula between San Jose and San Francisco. The greater slip along this portion of the San Andreas fault in the Random04 model accentuates the directivity effects, increasing the shaking intensities from MMI 7–8 to 8–9 for all of the hypocenters. North of Point Arena the opposite effect occurs; the Random04 slip distribution has less slip than that in Song2c, and the shaking intensities decrease by about one MMI unit. The decrease in rupture speed in the 100 km north of San Francisco for the random slip scenarios tends to decrease the shaking intensities from around 7–8 to around 6–7 in the vicinity of Santa Rosa, because subshear rupture directs less energy away from the fault compared with supershear rupture (Aagaard and Heaton, 2004).

In downtown San Francisco (site SF472, Figure 11) the velocity waveforms reaffirm the strong influence of the hypocenter. The amplitude and duration of shaking tend to correlate across hypocenter location much more so than across the slip distributions. The duration of strong shaking for the northern hypocenter (Scenario2cHypoN and ScenarioR04HypoN) is about 40 seconds compared to 15–20 seconds for the central and southern hypocenters (Scenario2cHypoC, ScenarioR04HypoC, Senario2cHypoS, and ScenarioR04HypoS), and as little as 15 seconds for

the 1906 hypocenter (SF1906Song2c and ScenarioR04Hypo06). The largest amplitude motions (with peak velocities of about 0.6 m/s) are associated with strong shear-wave directivity; this occurs in the four scenarios with the two hypocenters north of San Francisco (Rockport and Bodega Bay) and the southern hypocenter at San Juan Bautista (especially for the case of random slip). The southern hypocenter generates motion predominantly in the east-west direction whereas the hypocenters north of San Francisco generate motions in the east-west and north-south direction of about the equal amplitude. This difference cannot easily be tied to features in the source models because the slip distributions for the Song2c and Random04 models are significantly different and the rupture speeds in Scenario2cHypoN and Scenario2cHypoC are supershear immediately north of San Francisco but subshear in this same region for ScenarioR04HypoN and ScenarioR04HypoC.

The amplitude and duration of shaking is somewhat more consistent across the eight scenarios in San Jose (site SF474, Figure 12). The strongest shaking lasts about 40 seconds for the three hypocenters north of San Jose (Rockport, Bodega Bay, and 1906). The largest amplitude motions occur for the central and northern hypocenters, and the peak velocities reach 0.5 m/s many times over the 20 seconds of most intense shaking. In the case of the southern epicenter at San Juan Bautista, the rupture radiates most of the energy north of San Jose. In the Scenario2cHypoS simulation, the velocities are less than 0.2 m/s, but in the case of the random slip distribution, large slip on a portion of the rupture nearby does generate large amplitude motions with velocities reaching 0.4 m/s.

The simulations suggest that the ground motions in both Livermore (site SF292, Figure 13) and Santa Rosa (site SF501, Figure 14) from large events on the San Andreas fault are quite variable. For some hypocenters and slip distributions, the peak velocities fail to exceed 0.3 m/s. In other cases, such as Scenario2cHypoN, the peak velocities approach and may exceed 1 m/s at each location. The significant variations in amplitude and duration of motion can be attributed to both site and source effects. Some scenarios, such as Scenario2cHypoN and Scenario2CHypoS with supershear rupture and large slip north of San Francisco, radiate much more energy towards Livermore than the other scenarios. The Livermore basin amplifies the incoming surface waves and traps the energy, giving rise to large-amplitude, long-duration motions. Similarly, the Cotati and Windsor basins exhibit a strong influence on the motions in Santa Rosa. The northward propagating ruptures with large slip north of San Francisco in SF1906Song2c and Scenario2cHypos generate large Rayleigh waves that bounce around the basins resulting in a beating effect with two large pulses of energy spread over about 40 seconds.

The delta of the Sacramento and San Joaquin rivers sits about 40 km further away from the fault than Livermore, but at a similar location along the central portion of our ruptures. Consequently, the ground motions in the delta region (e.g., site CT06013301000, Figure 15) are strongly correlated with the rupture characteristics on this central portion. Scenario2cHypoN, with its southward supershear rupture propagation and large slips north of San Francisco, radiates more energy away from the fault along this central portion than the other scenarios. As a result the velocities in the

delta exceed 0.6 m/s with at least 90 seconds of strong shaking. Velocities exceeding 0.2 m/s with significant shaking lasting about 60 seconds are generated at this location in the delta for ScenarioR04HypoN, Scenario2cHypoC, and ScenarioR04HypoS, indicating that the large motions, as in the other locations, cannot be attributed to the distribution of slip or hypocenter alone. The ground motions for the other scenarios are smaller with peak velocities of about 0.1 m/s.

Eureka sits north of the northern extent of rupture and is in the forward directivity direction for all of the northward propagating ruptures. As a result, directivity effects control the amplitude and duration of the waveforms at this location (site SF172, Figure 16). For the SF1906Song2c, Scenario2cHypoC, and Scenario2cHypos simulations, the ruptures begin far enough south so that the ruptures within a couple hundred kilometers of Eureka are the same. That is, they all rupture towards the north with the same distribution of slip and the same rupture speed. This leads to nearly identical waveforms across the three scenarios; the velocity waveforms consist of velocity pulses with peak amplitudes exceeding 1.2 m/s with the intense shaking lasting about 20 seconds. Similarly, the waveforms for the ScenarioR04Hypo06, ScenarioR04HypoC, and ScenarioR04HypoS simulations are nearly identical, but in this case the peak velocities are about 0.6 m/s and the amplitudes exhibit a more pronounced decay over about 40 seconds.

Intensity in Urban Area

[AAGAARD]

The population density varies considerably over the region affected by earthquakes on the northern San Andreas fault. Some areas, such as the coastal areas north of San Francisco, are sparsely populated, where as other areas, such as the city of San Francisco, are densely populated. Figure 4 highlights the core urban area home to 65% of the 7 million people living in the San Francisco Bay area (2000 census). Most of the rest of the urban area, including Livermore, extends further east away from the San Andreas fault. In order to gauge the impact of large San Andreas fault earthquakes on the current population we want to characterize the shaking within this core urban area.

Figure 24 shows the fraction of this urban area where the shaking intensity exceeds a given level, computed from Aagaard's simulations for the scenarios with the 1906, central (Bodega Bay) and southern (San Juan Bautista) hypocenters. The curves further to the right correspond to scenarios where the intensities are higher for a given fraction of the urban area. Note that the actual regions associated with these intensities may be different from one scenario to another. MMI values of 7 and greater are associated with levels of shaking that can potentially cause moderate damage to modern structures.

Scenario2cHypoS subjects the smallest fraction of the urban area subjected to a given level of shaking. The 1906 earthquake ranks next lowest for MMI values above 7.5, yet MMI values exceed 7 over more than 70% of this core

urban area. The other four scenarios cause shaking at MMI of 8.5 or above over about 40% of this urban area and all of this urban area experiences shaking intensities of 7 or greater for the two scenarios with Bodega Bay epicenters. This suggests that ruptures initiating north of San Francisco and propagating southward tend to cause the strongest shaking over this core urban area. Overall, we find that most scenarios cause stronger shaking over the core San Francisco Bay urban area than the 1906 earthquake.

Discussion

[BROCHER]

[TO BE WRITTEN]

Simulations reaffirm importance of geologic structure in analyzing seismic hazard

Need to characterize shape (especially edges) and seismic wave speeds within the shallow basins of SF Bay area

Uncertainties in source that play a role in ground motions need to be constrained with better near-source data from variety of source geometries; would help improve characterization of seismic source in scenario modeling

Rise time & slip time function

Variation with depth, geodetic versus seismic slip

Spatial variability of slip, rupture speed, rise time and correlation between them

This simulation suite suggests that neither historic seismicity nor synthetic seismicity generated from a small number of rupture scenarios is sufficient to adequately predict future ground motion.

Resolving discrepancies in magnitude in matching b/t Song source model and Boatwright and Bundock intensities

See Segall notes on constraining depth extent of rupture

Increasing depth extent of slip with double the rise time results in Mw 7.9 event with only small increase in misfit.

Impact of large San Andreas earthquakes occurring today

Delta Region/Sacramento

Of particular interest is the simulated ground motion in the Sacramento-San Joaquin Delta Region. This region, once a sea-level marsh, now encompasses approximately 3000 square kilometers of reclaimed land and is heavily used for agricultural purposes. Pumping since the 1800's has lowered the groundwater table and produced farmland. Subsidence caused by the consolidation of sediments and the decomposition of peat has caused much of the western

and central parts of the delta to be 5–8 meters below sea level. A 1500-kilometer levee system now protects this region. Constructed primarily of unconsolidated sediments, the levees are subject to liquefaction and failure from strong ground motions. Sudden failure of one or more levees would cause immediate flooding. Depending on the severity, levee failure could paralyze California's water supply and have catastrophic economic and social consequences. Hence, it is important to assess historic and scenario ground motions in this region. The probability of an event similar to Scenario2cHypoN is relatively small. The Working Group on California Earthquake Probabilities [WGCEP, 2003] estimated a 4.7% probability of a 1906-like event along the San Andreas fault during the 30 year period between 2002 and 2031. This suggests that the 30-year likelyhood of a M7.8 - M7.9 earthquake initiating on the northern segment of San Andreas fault with a specific rupture model capable of producing high amplitude ground motions in the delta is no greater than about 1

Urban Area

Intensities are high enough than modern structures could be potentially damaged across about ??% of the core San Francisco Bay urban area (which generally lies between the San Andreas and Hayward faults). Regions with higher intensities (where damage would be more widespread and severe) vary from scenario to scenario, but expect about ??–??% of the region to experience shaking cooresponding to MMI values of 8 and greater. Any of the earthquakes in our suite of scenarios would have a severe economic impact on core urban area [or something like that].

Impact of Mw 7.9 is about the same as Mw 7.3

Don't need 500 km long rupture to create strong shaking across entire SF Bay area (scenarios with hypocenters at Bodega Bay or further south illustrate this)

SF Bay area is all within a few tens of km of rupture

Areas between San Andreas and Hayward faults appear to be most vulnerable to strong shaking (accounts for about 2/3 of urban population)

Need to look forward and understand ground motions from events expect in the next 30+ years

Suites of scenarios to characterize median and variability of shaking

Could be used to help identify areas where retrofit of structures would have higher priority

Conclusions

[TO BE WRITTEN]

Acknowledgments

Howard Bundock and Jack Boatwright (ShakeMap processing)

Seok Goo Song (source model)

David Wald (discussions)

Larry Baker (cluster support)

References

Aagaard, B. T., T. M. Borcher, D. Dolenc, D. Dreger, A. Frankel, R. W. Graves, S. Harmsen, S. Hartzell, S. Larsen, and M. L. Zoback (2008). Ground motion modeling of the 1906 San Francisco earthquake I: Validation using the 1989 Loma Prieta earthquake. submitted to Bulletin of the Seismological Society of America.

Aagaard, B. T. and T. H. Heaton (2004, December). Near-source ground motions from simulations of sustained intersonic and supersonic fault rupture. *Bulletin of the Seismological Society of America 94*(6), 2064–2078.

Anooshehpoor, A., T. H. Heaton, B. P. Shi, and J. N. Brune (1999, August). Estimates of the ground accelerations at Point Reyes Station during the 1906 San Francisco earthquake. *Bulletin of the Seismological Society of America 89*(4), 845–853.

Boatwright, J. and H. Bundock (2005). Modified Mercalli Intensity maps for the 1906 San Francisco earthquake plotted in ShakeMap format. Technical Report Open-File Report 2005-1135, U.S. Geological Survey. http://pubs.usgs.gov/of/2005/1135/.

Boore, D. M. (1977, June). Strong-motion recordings of the California earthquake of April 18, 1906. *Bulletin of the Seismological Society of America 67*(3), 561–577.

Borcherdt, R. D. and J. F. Gibbs (1976, April). Effects of local geological conditions in the San Francisco Bay region on ground motions and the intensities of the 1906 earthquake. *Bulletin of the Seismological Society of America 66*(2), 467–500.

Day, S. M. (1982, December). Three-dimensional simulation of spontaneous rupture: The effect of nonuniform prestress. *Bulletin of the Seismological Society of America 72*(6), 1881–1902.

Hisada, Y. (2001, August). A theoretical omega-square model considering spatial variation in slip and rupture velocity. Part 2: Case for a two-dimensional source model. *Bulletin of the Seismological Society of America 91*(4), 651–666.

Kagawa, T., K. Irikira, and P. G. Somerville (2004). Differences in ground motion and fault rupture process between the surface and buried rupture earthquakes. *Earth, Planets, and Space 56*(1), 3–14.

Lawson, A. and H. Reid (Eds.) (1908). *The California earthquake of April 18, 1906. Report of the State Earthquake Investigation Commission*. Washington, D.C.: Carnegie Institution of Washington. in two volumes and atlas.

Lomax, A. (2005, June). A reanalysis of the hypocentral location and related observations for the great 1906 California earthquake. *Bulletin of the Seismological Society of America 95*(3).

Mai, P. M. and G. C. Beroza (2002, November 10). A spatial random field model to characterize complexity in earthquake slip. *Journal of Geophysical Research - Solid Earth 107*(B11).

McPhee, D. K., V. E. Langenheim, S. Hartzell, R. J. McLaughlin, B. T. Aagaard, R. C. Jachens, and C. McCabe (2008). Basin structure beneath the Santa Rosa Plain, northern California: Implications for damage caused by the 1969 Santa Rosa and 1906 San Francisco earthquakes. submitted to Bulletin of the Seismological Society of America.

Nilsson, S., N. A. Petersson, B. Sjögreen, and H. O. Kreiss (2006). Stable difference approximations for the elastic wave equation in second order formulation. Technical Report Technical Report UCRL-JRNL-222276, Lawrence Livermore National Laboratory. 39 pages.

Somerville, P. G., K. Irikura, R. Graves, S. Sawada, D. Wald, N. Abrahamson, Y. Iwasaki, T. Kagawa, N. Smith, and A. Kowada (1999, January/February). Characterizing crustal earthquake slip models for the prediction of strong ground motion. *Seismological Research Letters 70*(1), 199–222.

Song, S. G., G. C. Beroza, and P. Segall (2008). A unified source model for the 1906 San Francisco earthquake. *Bulletin of the Seismological Society of America*.

Thatcher, W., M. Grant, and M. Lisowski (1997). Resolution of fault slip along the 470-km-long rupture of the great 1906 San Francisco earthquake and its implications. *Journal of Geophysical Research - Solid Earth 102*(B3), 5353–5368.

Wald, D., B. Worden, V. Quitoriano, and K. Pankow (2005, May). *ShakeMap Manual: Technical Manual, Users Guide, and Software Guide* (Version 1.0 ed.). United States Geological Survey. http://pubs.usgs.gov/tm/2005/12A01/.

Wald, D. J., H. Kanamori, D. V. Helmberger, and H. T. H. (1993, August). Source study of the 1906 San Francisco earthquake. *Bulletin of the Seismological Society of America 83*(4), 981–1019.

Ward, S. N. (2000, April). San Francisco Bay Area earthquake simulations: A step toward a standard physical earthquake model. *Bulletin of the Seismological Society of America 90*(2), 370–386.

U.S. Geological Survey, MS977
345 Middlefield Rd.
Menlo Park, CA 94025
(B.T.A., T.M.B., M.L.Z.)

U.S. Geological Survey, MS966
P.O. Box 25046
Golden, CO 80225
(A.F., S.H., S.H.)

Seismological Laboratory
University of California, Berkeley
215 McCone Hall
Berkeley, CA 94720
(D.D.)

URS Corporation
566 El Dorado St.
Pasadena, CA 91101
(R.W.G.)

Lawrence Livermore National Laboratory
Box 808, L-103
Livermore, CA 94551-0808
(S.L.)

Lawrence Livermore National Laboratory
Box 808, L-???
Livermore, CA 94551-0808

(K.M., S.N., A.R. B.S., H.T.)

Lawrence Livermore National Laboratory
Box 808, L-550
Livermore, CA 94551-0808
(N.A.P.)

Prepared by LLNL under Contract DE-AC52-07NA27344.

Table 1. Numerical Models

	Aagaard	Graves	Harmsen *et al.*	Larsen *et al.*	Petersson *et al.*
Domain					
Length	250 km	555 km	128 km	630 km	550 km
Width	110 km	162 km	52 km	320 km	200 km
Max. depth	40 km	45 km	31 km	55 km	40 km
NW corner	-123.7083, 38.2832	-125.5000, 40.2000	-122.7313, 37.6313	-126.2037, 39.6589	-125.4990, 40.0440
NE corner	-122.7002, 38.8944	-123.9482, 41.0505	-122.3116, 37.9610	-123.2940, 41.3485	-123.6000, 41.1000
SE corner	-121.0208, 37.0716	-120.2911, 36.9623	-121.2978, 37.1331	-119.0100, 36.7700	-119.9590, 37.1030
SW corner	-122.0180, 36.4894	-121.8528, 36.1118	-121.7173, 36.8069	-121.8819, 35.0804	-121.8060, 36.0470
Projection	none (3-D Earth)	??	ellipsoidal transverse Mercator	??	??
Discretization	unstructured FE	staggered-grid FD	staggered-grid FD	staggered-grid FD	node-centered FD
Space	2nd order	4th order	4th order	4th order	2nd order
Time	2nd order	2nd order	2nd order	2nd order	2nd order
Resolution	variable	150 m	50 m, 150 m	100 m	125 m
Bandwidth	T > 2.0 s	T > 1.0 s	T > 1.0 s	T > 1.0 s	T > 2.0 s
Min. Vs	700 m/s	760 m/s	330 m/s	500 m/s	500 m/s
Features					
Topography	yes	“bulldozed”	“squashed”	yes	“bulldozed”
Water	air filled	sediment filled	excluded	included	included
Mat. Properties	USGS 05.1.0	USGS 05.1.0	USGS 05.1.0	USGS 05.1.0	USGS 05.1.0
Attenuation	no	Graves	Graves	USGS VM 05.1.0	no
Eq source	offset in mesh	point sources	point sources	point sources	point sources
# pt. sources	N/A	??	??	??	12,313 (Song2c)
Fault surface	3-D geologic model	3-D geologic model	3-D geologic model	3-D geologic model	3-D geologic model

The corners of the bounding boxes of each domain are given in longitude and latitude (WGS84 horizontal datum).

Table 2. Description of Earthquake Simulations

Simulation Label	Slip Distribution	Hypocenter
SF1906Song2	Song2	1906
SF1906Song2c	Song2c	1906
Scenario2cHypoN	Song2c	Rockport
Scenario2cHypoC	Song2c	Bodega Bay
Scenario2cHypoS	Song2c	San Juan Bautista
ScenarioR04Hypo06	Random04	1906
ScenarioR04HypoN	Random04	Rockport
ScenarioR04HypoC	Random04	Bodega Bay
ScenarioR04HypoS	Random04	San Juan Bautista

Song2 produces a moment magnitude 7.9 event (average slip is 4.3 m), whereas Song2c and Random04 produce a moment magnitude 7.8 event (average slip is 3.0 m). Hypocenter locations are given in Table 3.

Table 3. Hypocenter Locations

Hypocenter	Longitude	Latitude
1906	-122.55	37.75
Rockport	-124.000	39.800
Bodega Bay	-123.016	38.300
San Juan Bautista	-121.615	36.872

All hypocenters are at an elevation of -10 km. Longitude and latitude are given in the WGS84 horizontal datum.

Table 4. Locations of Velocity Waveform Sites

Site Label	Location	Longitude	Latitude
SF172	Eureka	-124.1625	40.8022
SF292	Livermore	-121.7669	37.6819
SF472	San Francisco	-122.4183	37.7750
SF474	San Jose	-121.8939	37.3394
SF501	Santa Rosa	-122.7133	38.4406
CT06013301000	Sacramento Delta	-121.6301	38.0383

Site CT06013301000 is the centroid of census track 06013301000. The other sites correspond to Boatwright and Bundock (2005) intensity sites.

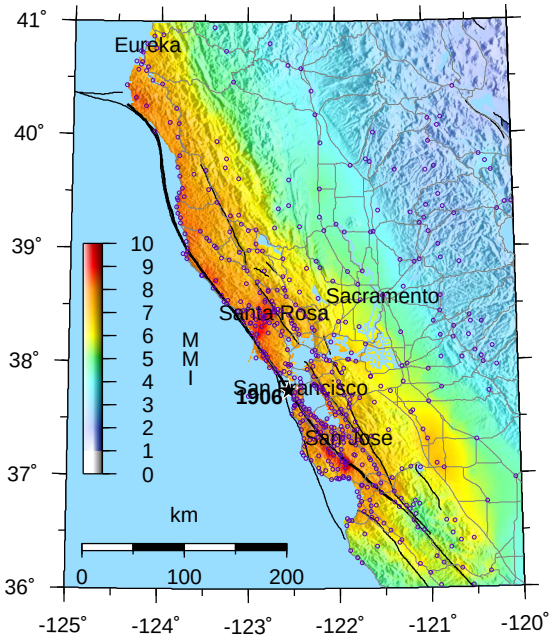

Figure 1. ShakeMap for the 1906 San Francisco earthquake based on the Boatwright and Bundock (2005) intensities (processed 2005/10/18). Open circles indentify the intensity sites used to construct the ShakeMap.

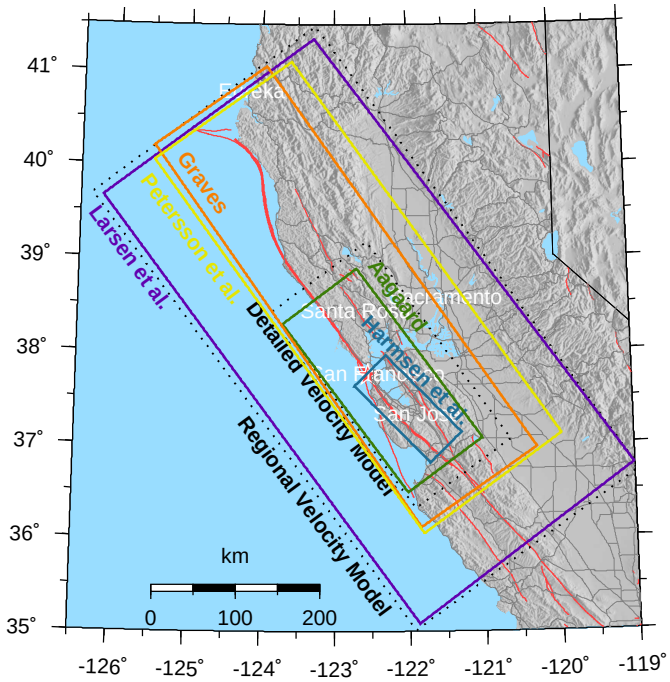

Figure 2. Bounding boxes of the domains used by the five ground motion modeling groups and the detailed and regional portions of the USGS Bay Area Velocity Model 05.1.0. The thick red line shows the surface trace of the San Andreas fault, the white star identifies the epicenter, and the thin red lines delineate the surface traces of the major faults in the region.

ADD PLOT HERE: Song2

ADD PLOT HERE: Song2c

ADD PLOT HERE: Random04HypoN

Figure 3. Source models for three of the scenarios. The top panel shows the Song2 source model, the middle panel the Song2c source model, and the bottom panel the Random04HypoN source model. The colors depict the magnitude of right-lateral slip and the contours show slip initiation time (contour interval is ?? s). The nonplanar fault geometry has been mapped onto a rectangular grid for plotting purposes.

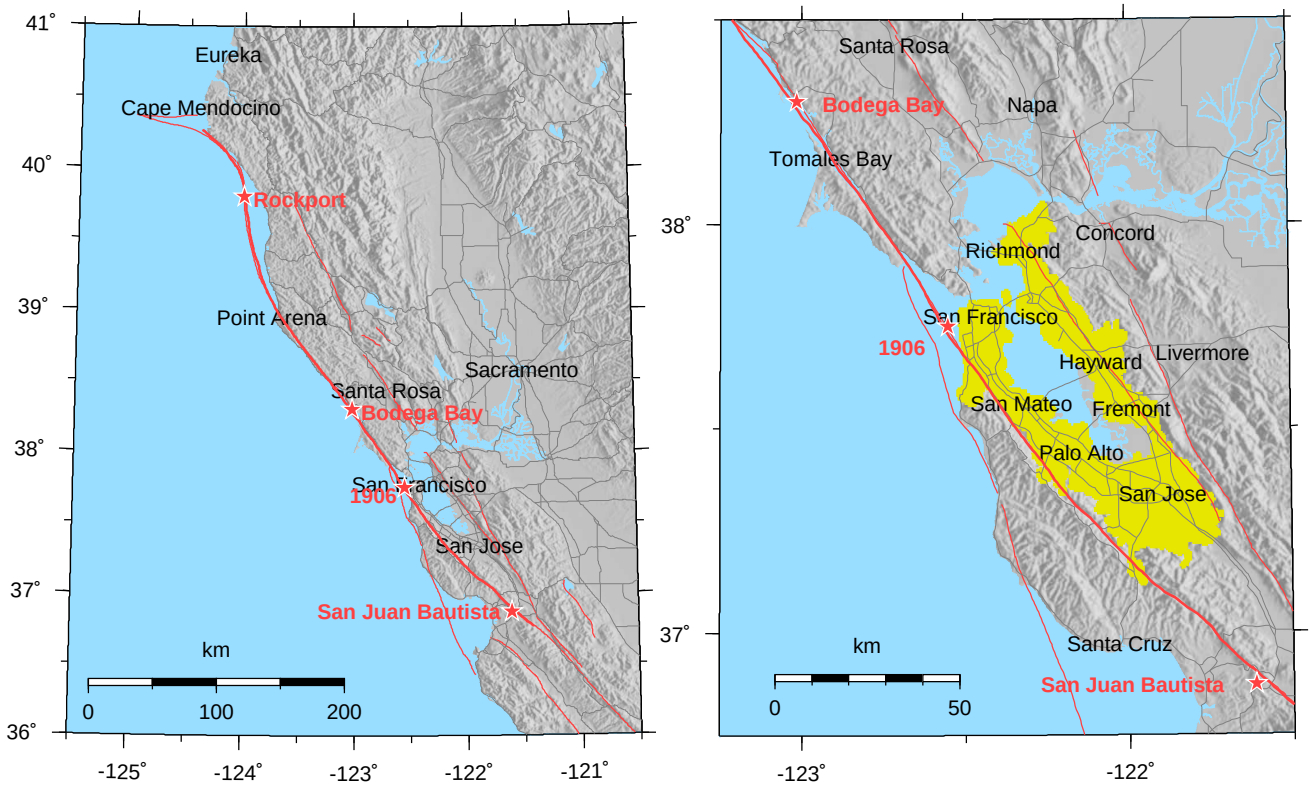

Figure 4. Map of scenario epicenters as viewed on maps of the entire rupture length (left) and the San Francisco Bay vicinity (right). The thick red line delineates the extent of ruptures in the simulations and the red stars denote the 1906 and scenario epicenters. The yellow highlighted region is the main San Francisco Bay urban area in the vicinity of the San Andreas and Hayward faults.

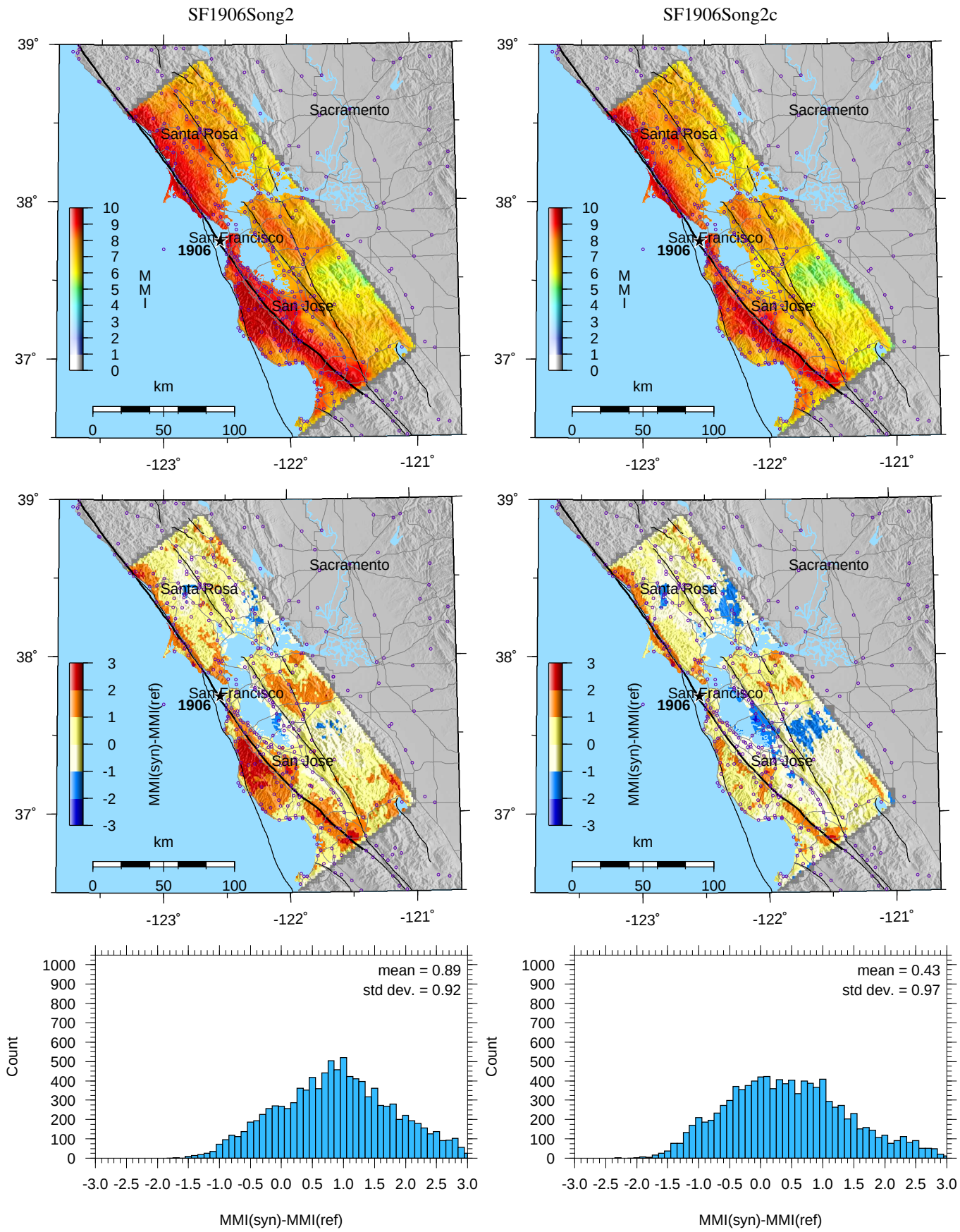

Figure 5. ShakeMaps for Aagaard's simulations (T > 2.0 s) of the 1906 earthquake using the Song2 (left) and Song2c (right) source models. Open circles indentify the Boatwright and Bundock intensity sites. Lower panels show comparisons of the synthetic ShakeMaps with respect to the Boatwright and Bundock ShakeMap.

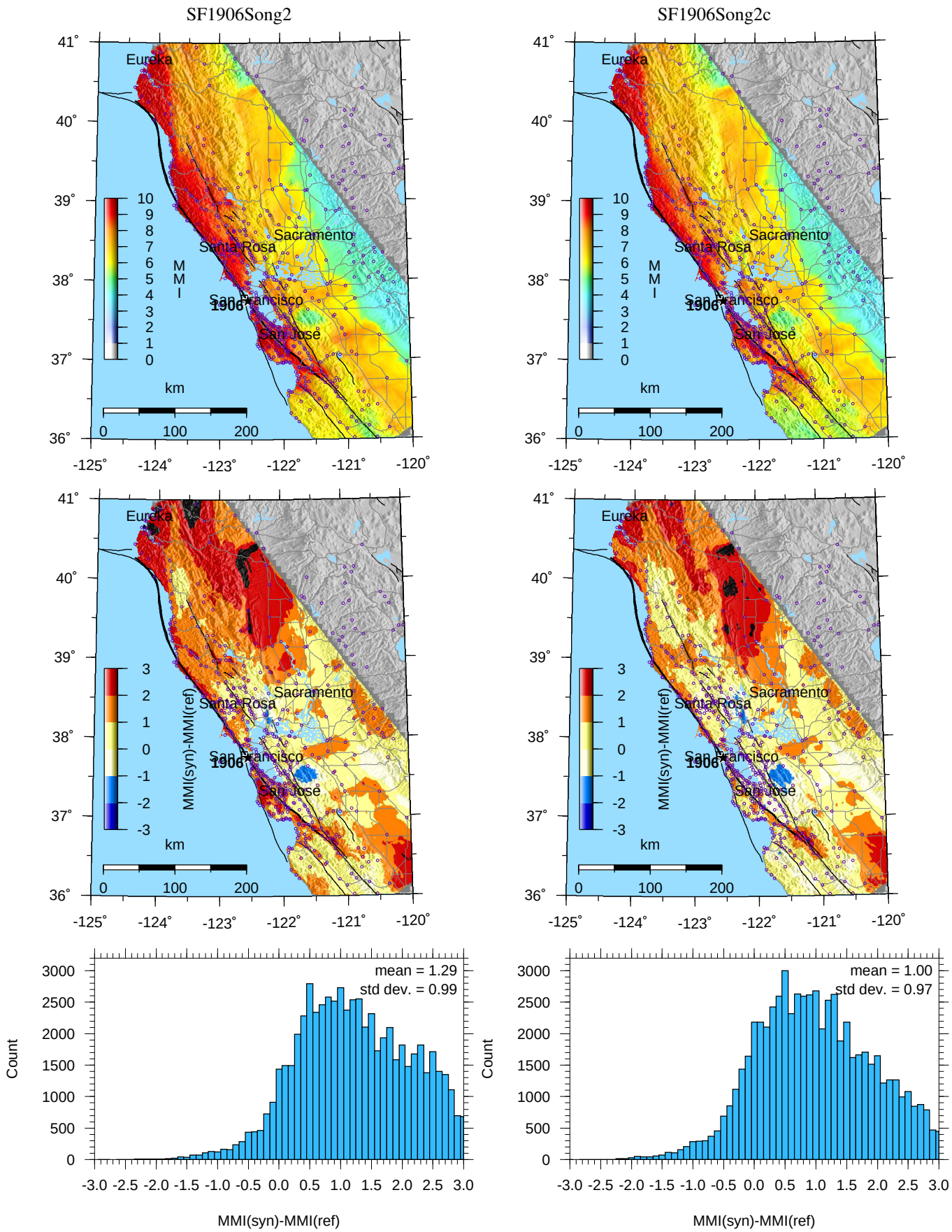

Figure 6. ShakeMaps for Larsen *et al.*'s simulations (T > 1.0 s) of the 1906 earthquake using the Song2 (left) and Song2c (right) source models. Open circles indentify the Boatwright and Bundock intensity sites. Lower panels show

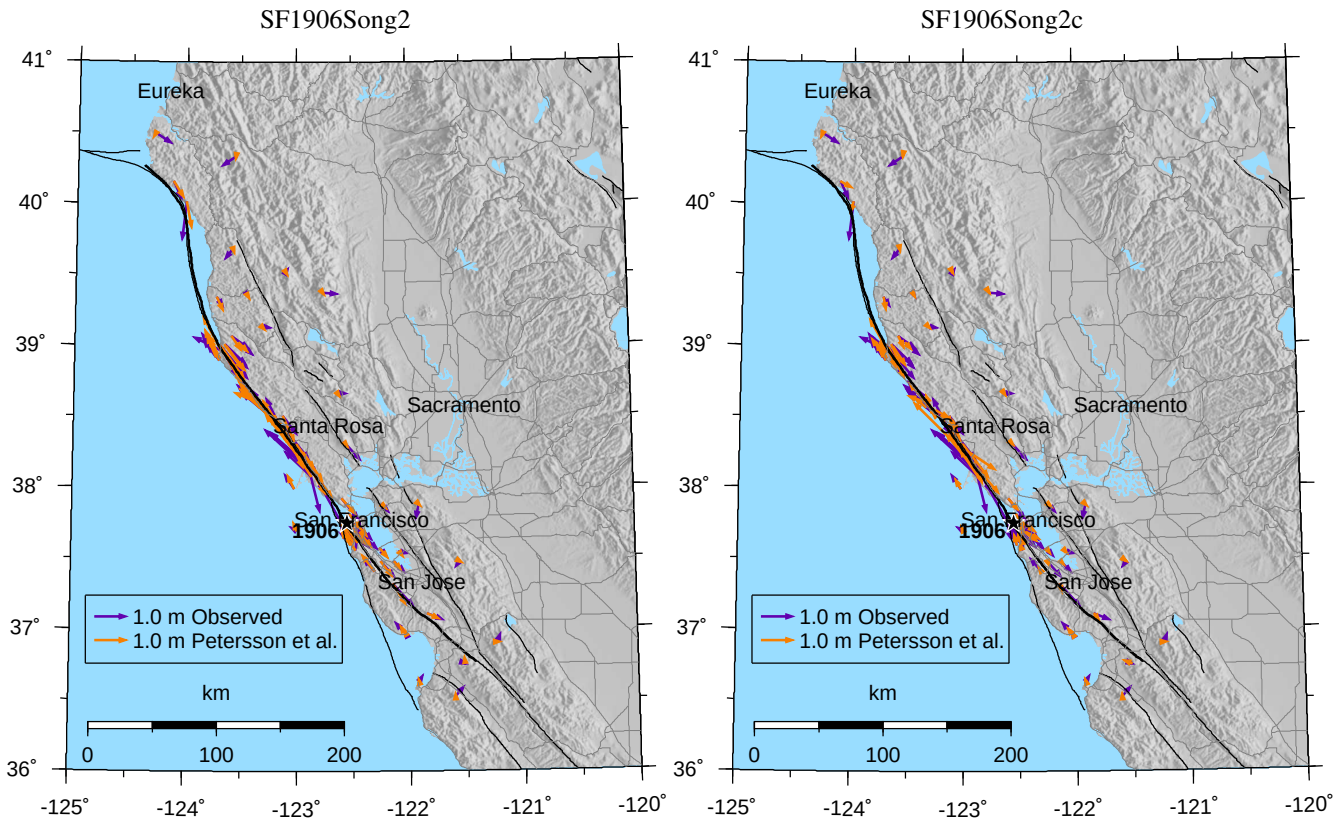

Figure 7. Comparison of geodetic displacements for Petersson *et al.*'s simulations of the 1906 earthquake using the Song2 (left) and Song2c (right) source models with respect to the displacements inferred by Song *et al.* from triangulation measurements.

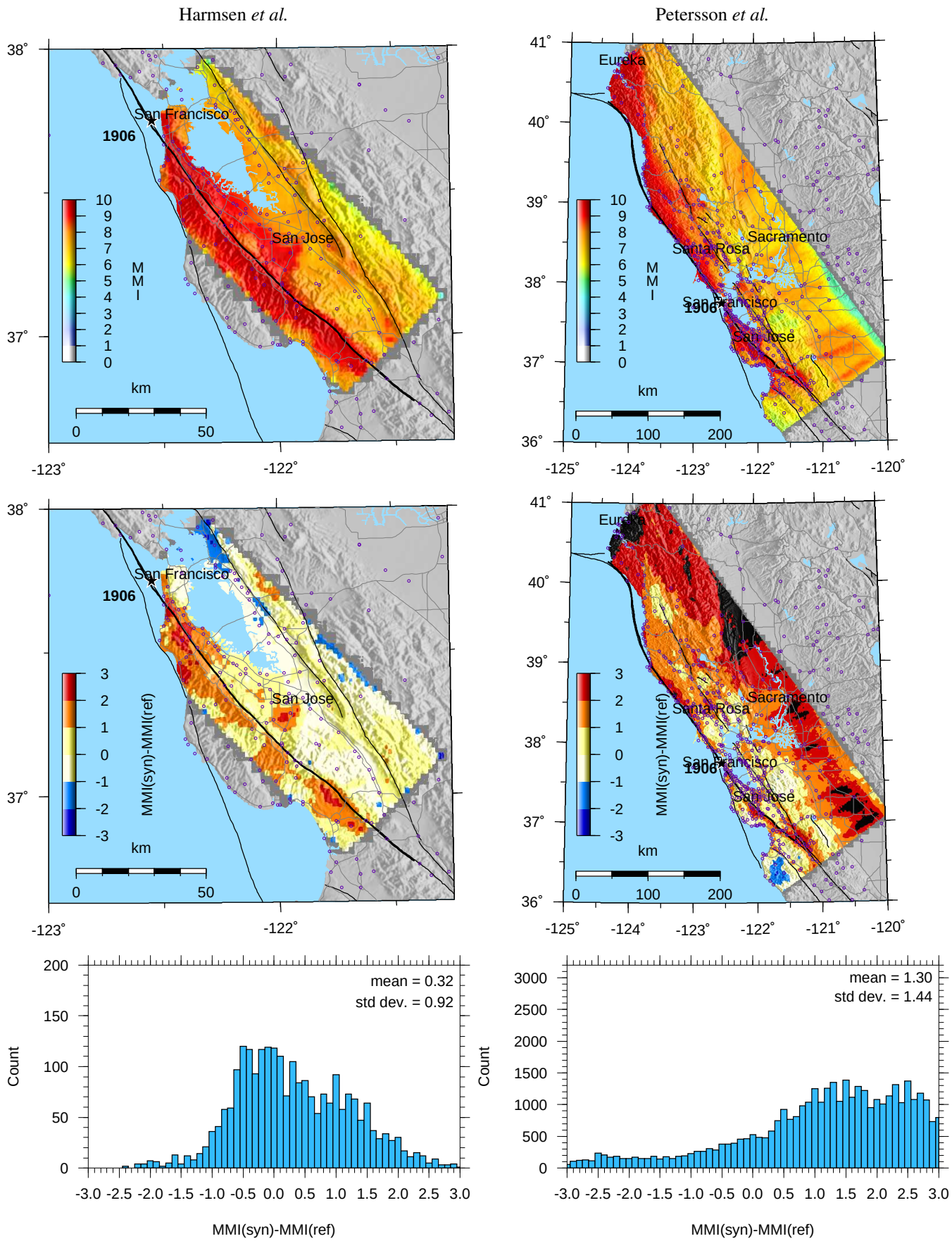

Figure 8. ShakeMaps for Harmsen *et al.*'s simulation (T > 1.0 s) and Petersson *et al.*'s simulation (T > 2.0 s) of the 1906 earthquake using the Song2c source model. Open circles indentify the Boatwright and Bundock intensity sites.

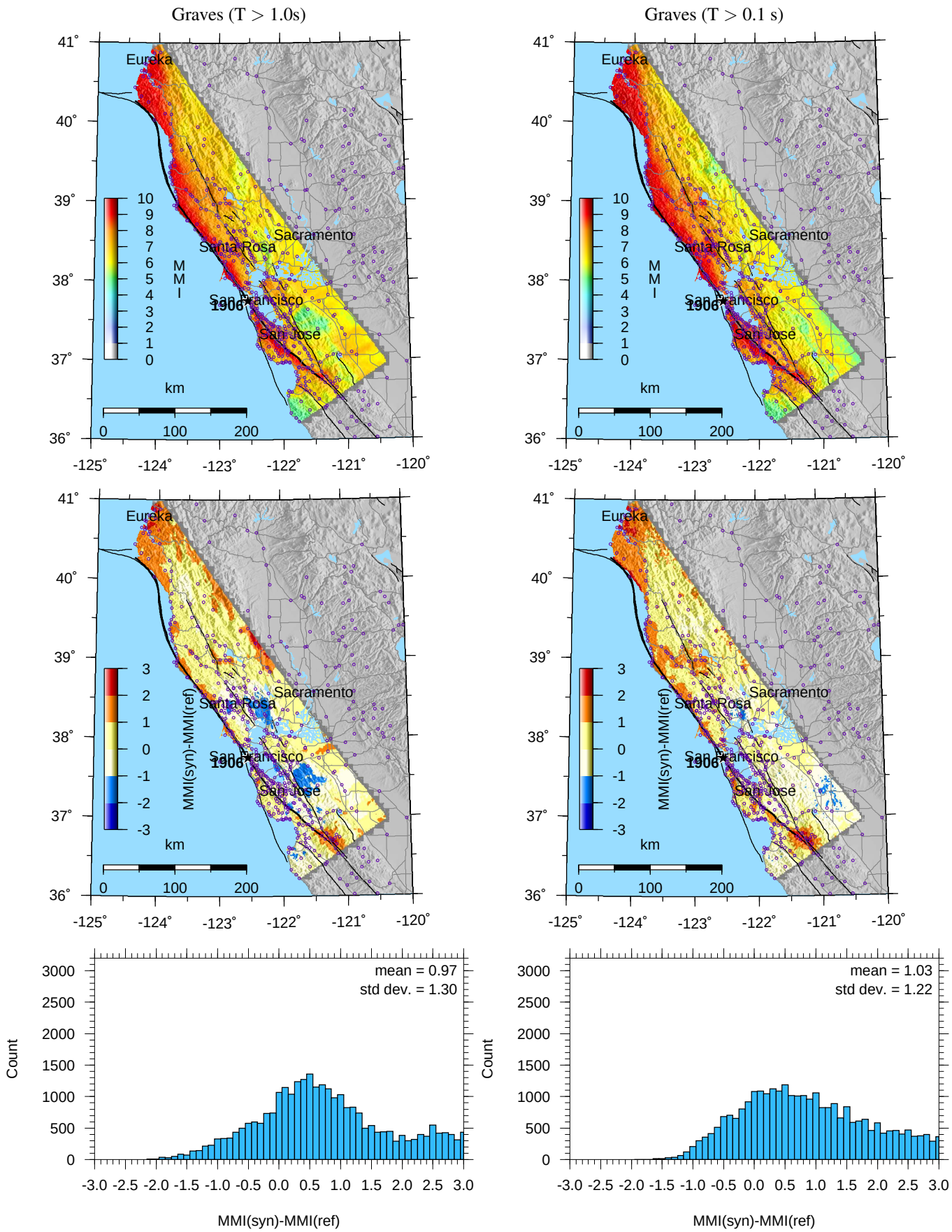

Figure 9. ShakeMaps for Graves's long-period (left) and broadband (right) simulations of the 1906 earthquake using the Song2c source model. Open circles indentify the Boatwright and Bundock intensity sites. Lower panels show

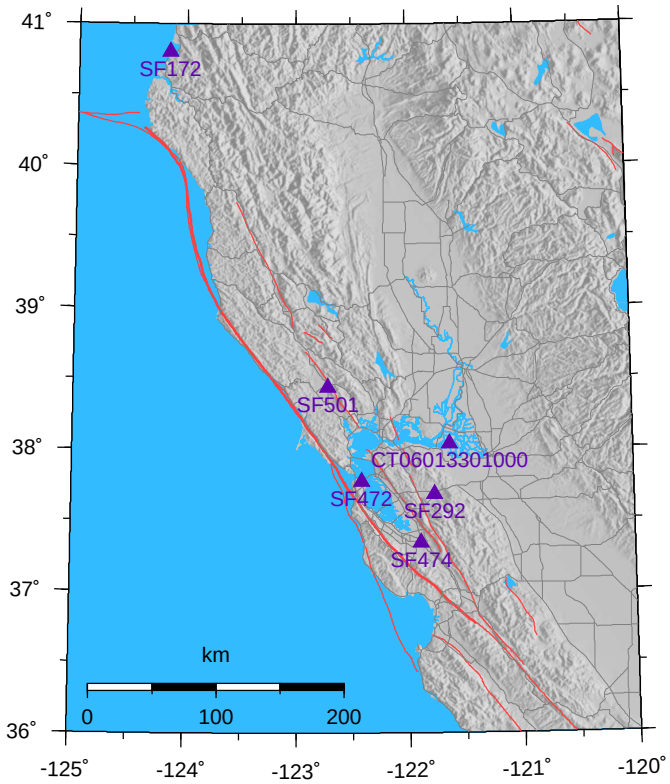

Figure 10. Locations of the six sites used in the comparison of velocity waveforms.

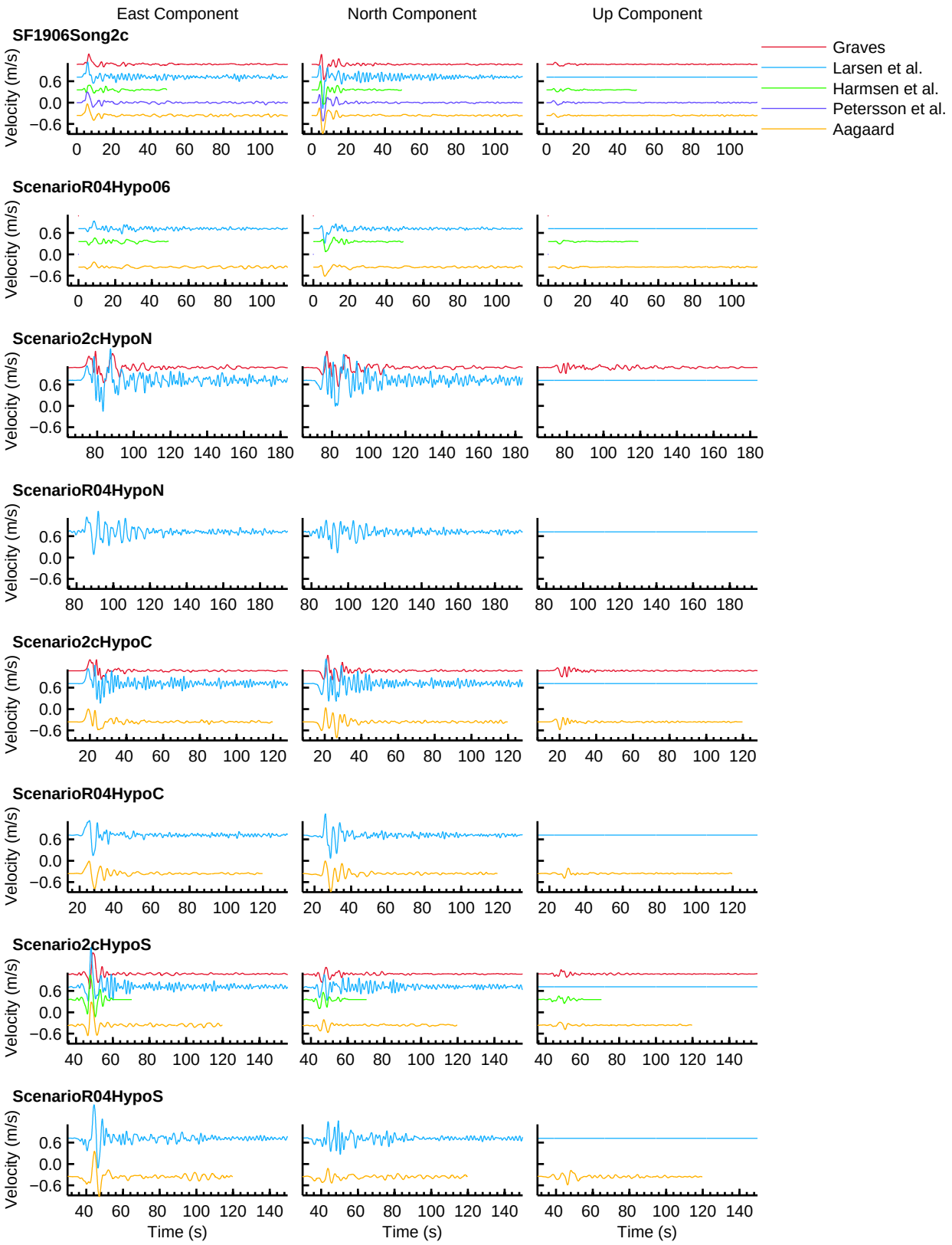

Figure 11. Comparison of velocity waveforms in downtown San Francisco (site SF472). All waveforms have been low-pass filtered to a bandwidth of T > 2.0 s.

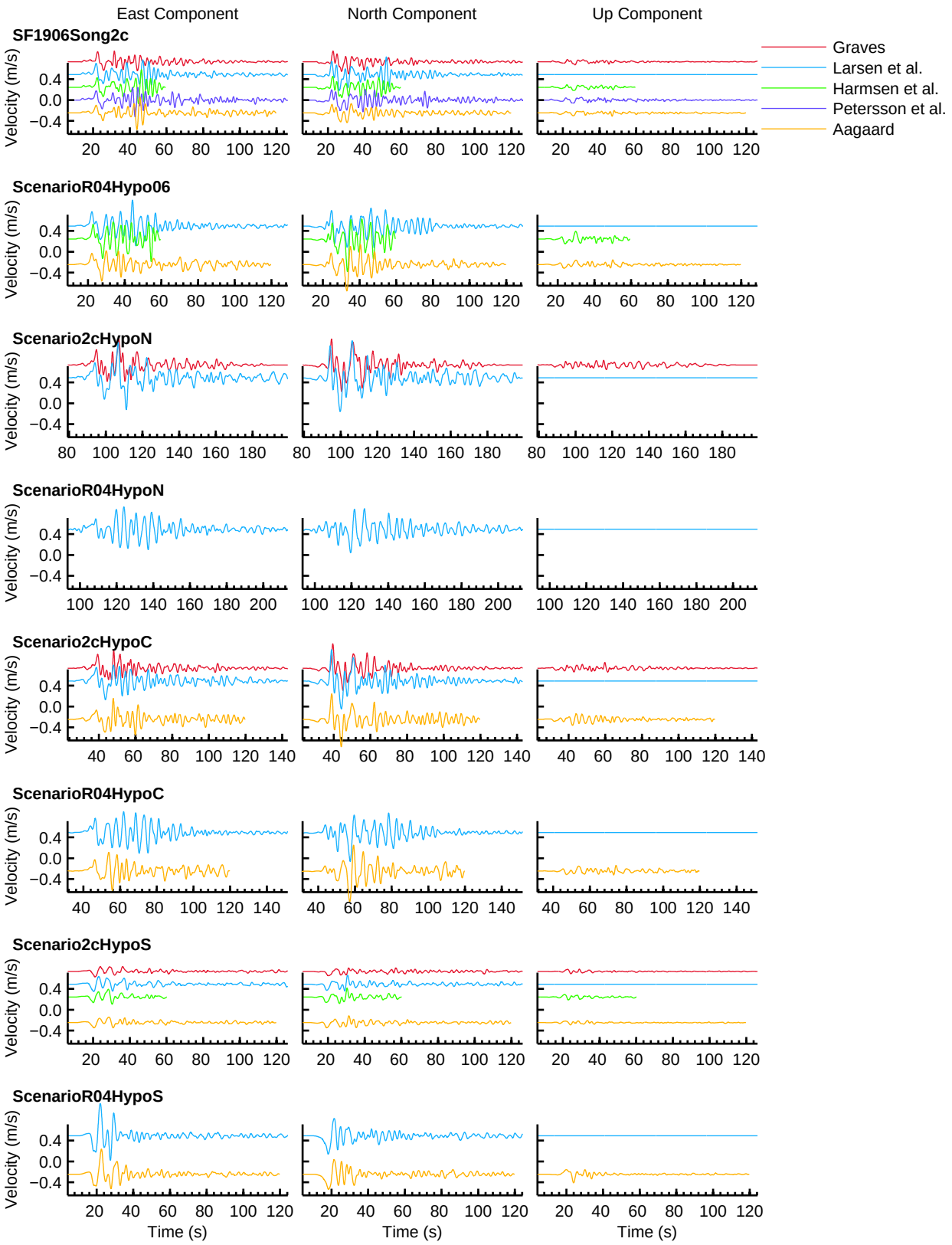

Figure 12. Comparison of velocity waveforms in downtown San Jose (site SF474). All waveforms have been low-pass filtered to a bandwidth of T > 2.0 s.

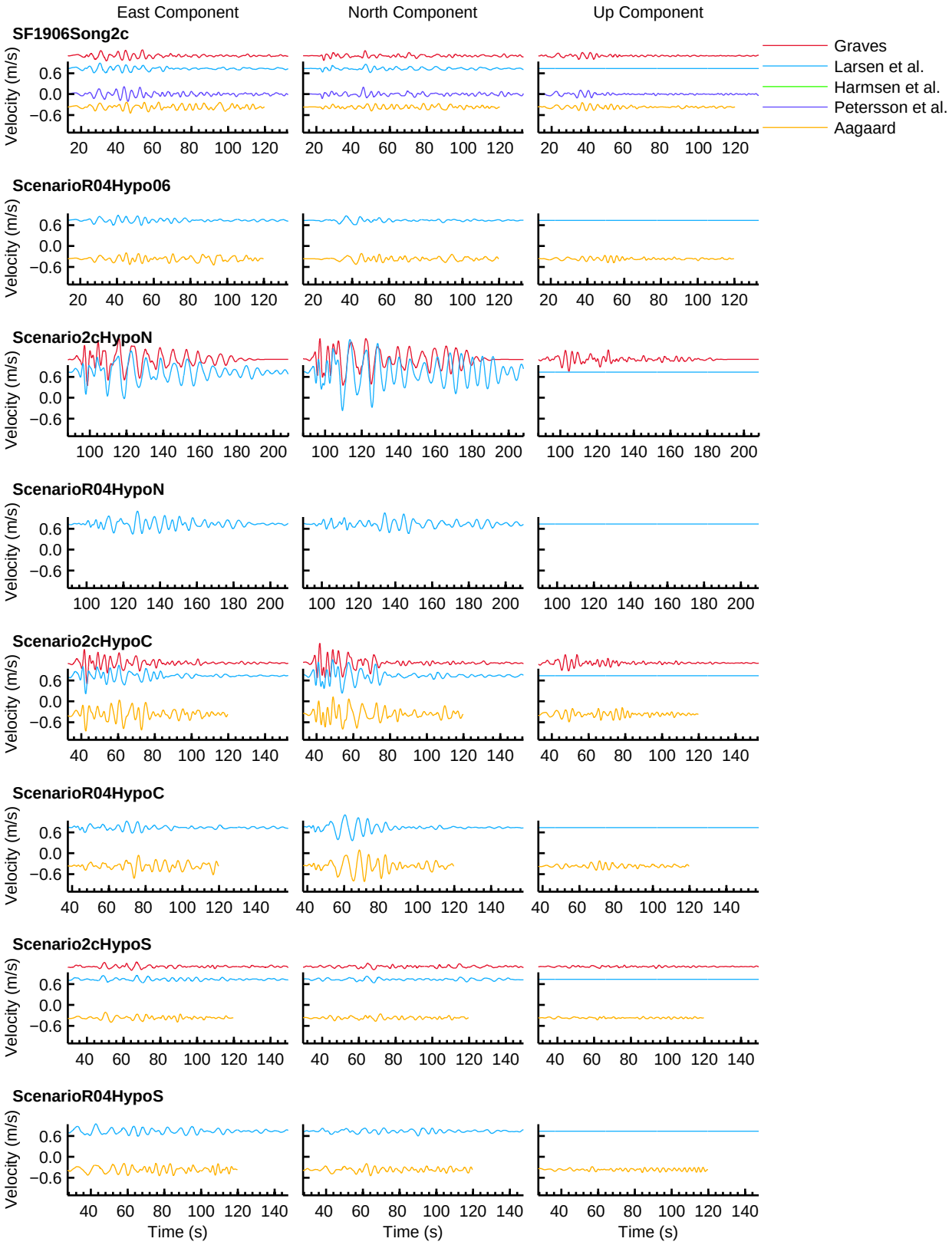

Figure 13. Comparison of velocity waveforms in Livermore (site SF292). All waveforms have been low-pass filtered to a bandwidth of T > 2.0 s.

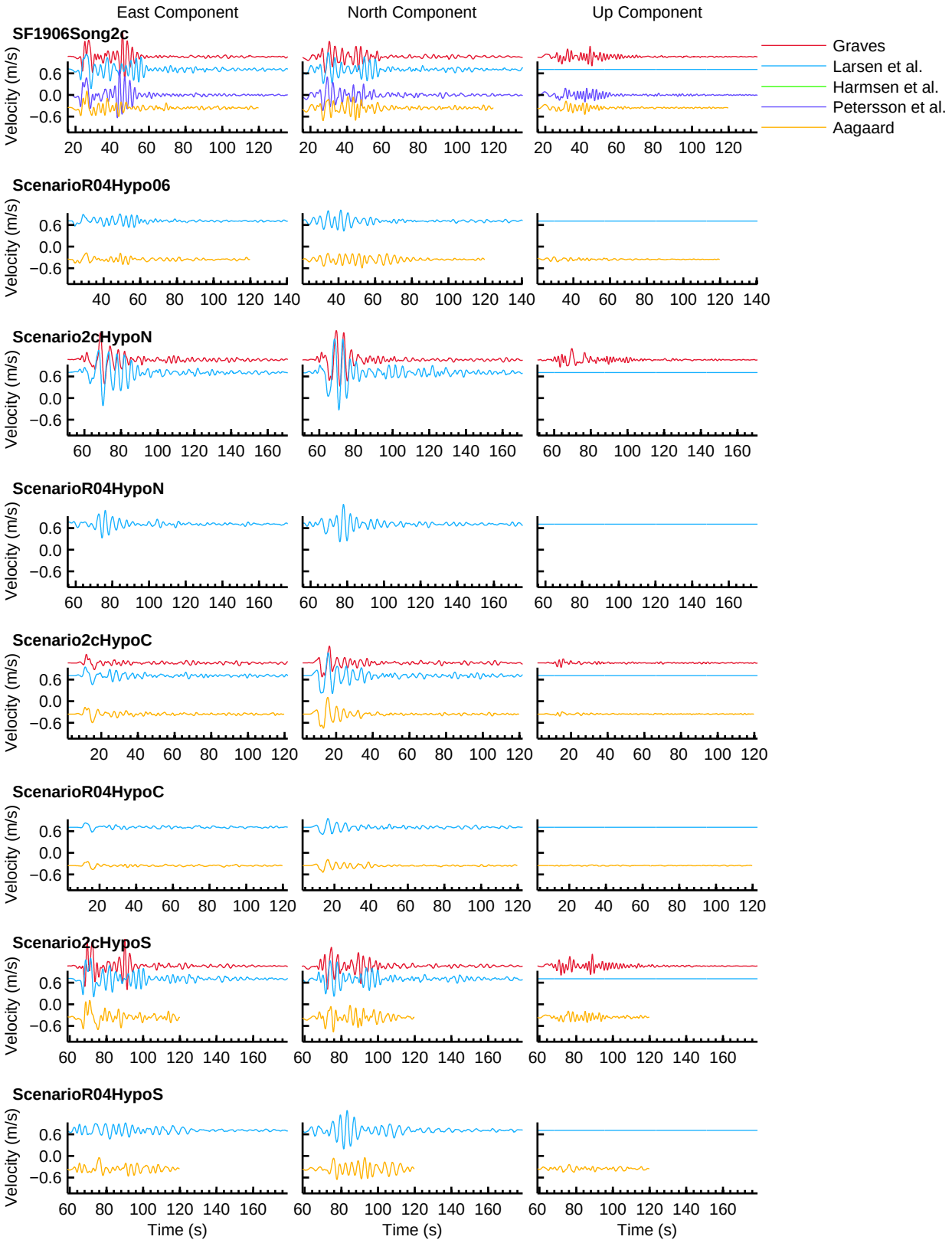

Figure 14. Comparison of velocity waveforms in Santa Rosa (site SF501). All waveforms have been low-pass filtered to a bandwidth of T > 2.0 s.

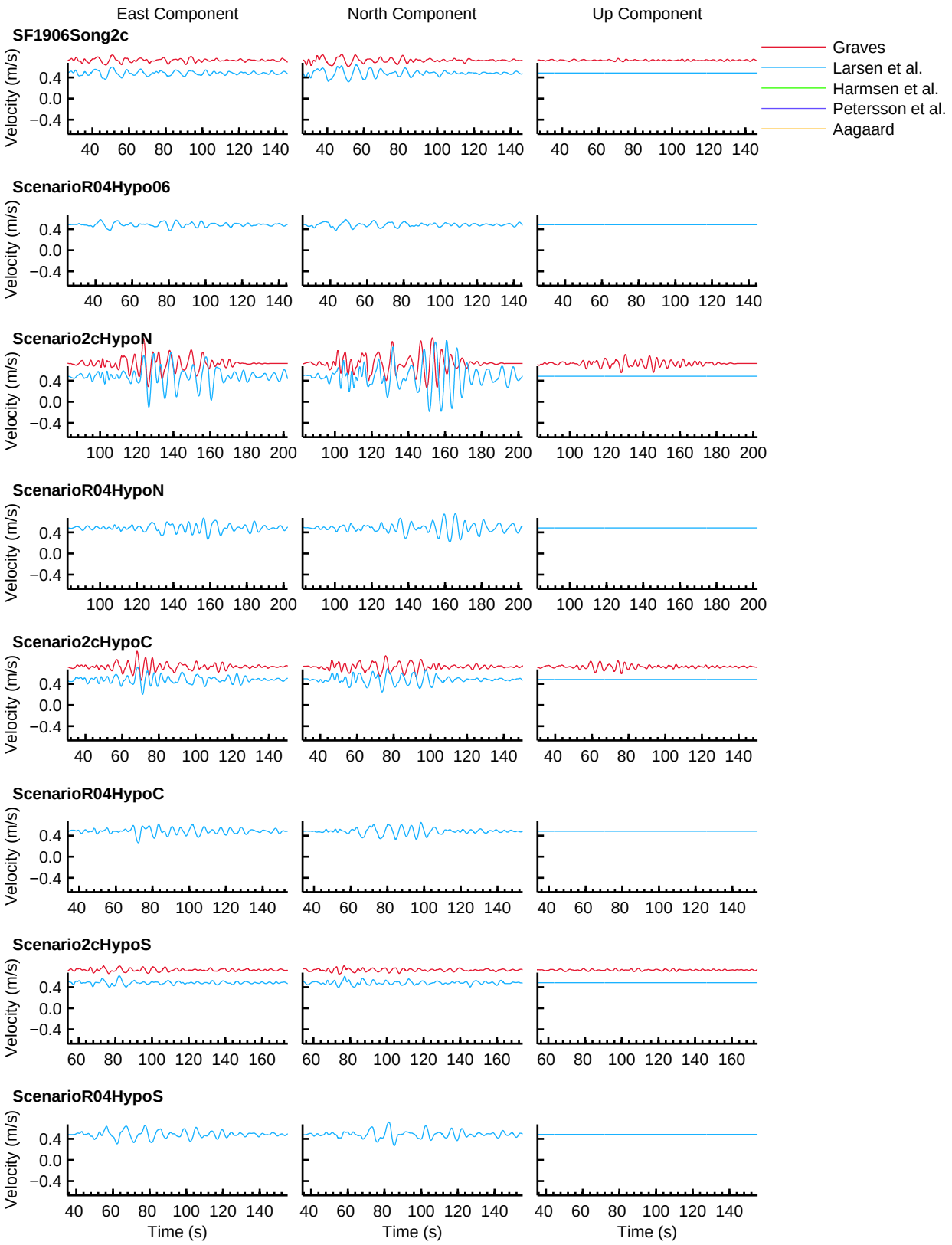

Figure 15. Comparison of velocity waveforms in the Sacramento-San Joaquin delta (site CT06013301000). All waveforms have been low-pass filtered to a bandwidth of T > 2.0 s.

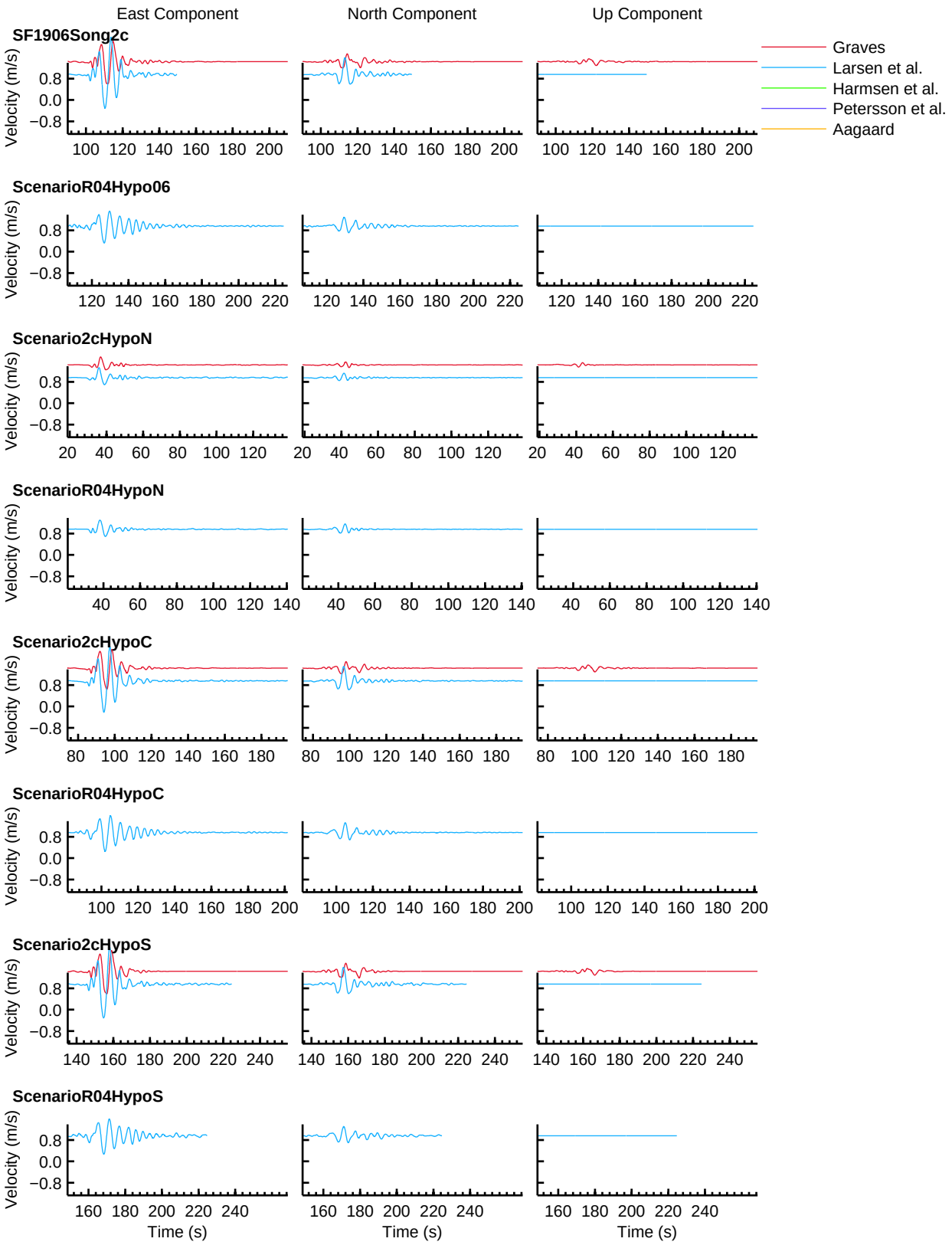

Figure 16. Comparison of velocity waveforms in Eureka (site SF172). All waveforms have been low-pass filtered to a bandwidth of T > 2.0 s.

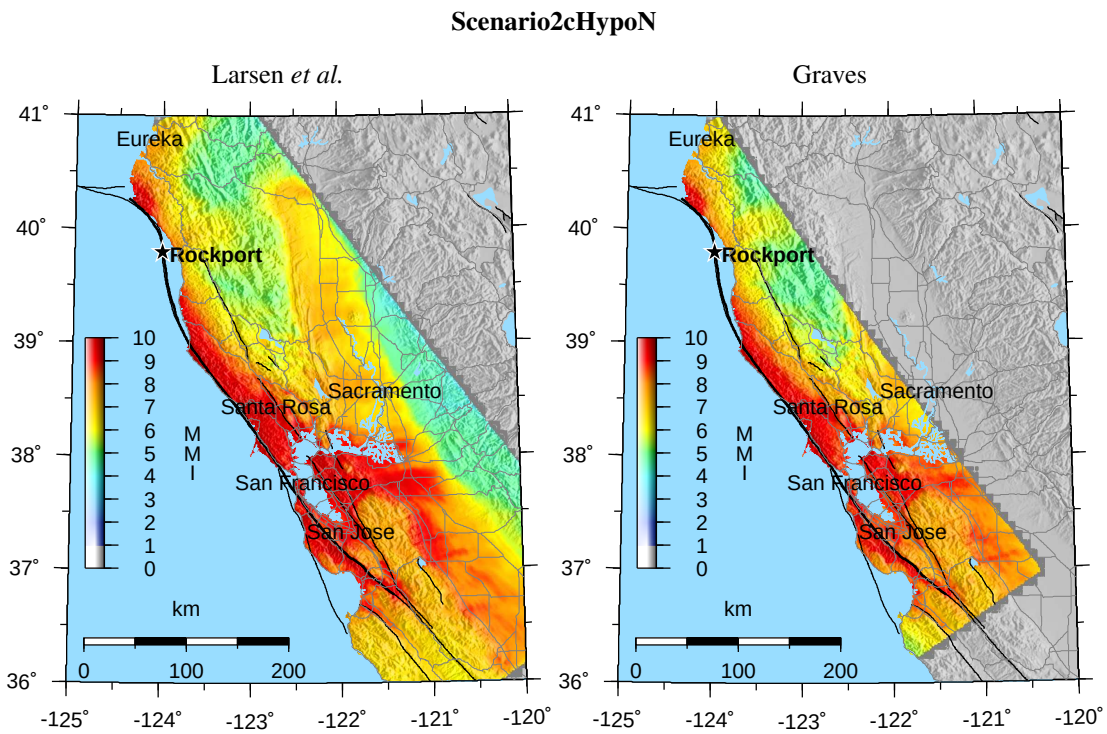

Figure 17. ShakeMaps for Larsen *et al.*'s (T > 1.0 s, left) and Graves (T > 1.0 s, right) Scenario2cHypoN simulations. The thick black line delineates the rupture extent and the black star identifies the epicenter.

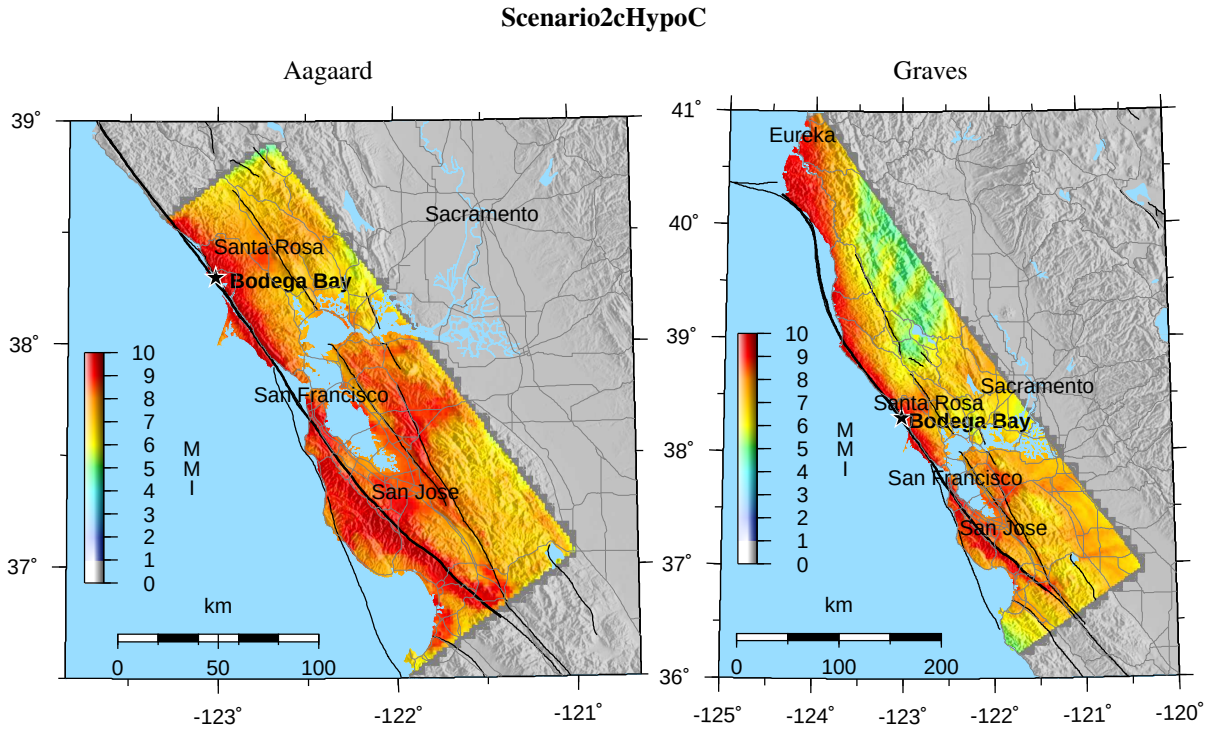

Figure 18. ShakeMaps for Aagaard's (T > 2.0 s, left) and Graves (T > 1.0 s, right) Scenario2cHypoC simulations. The thick black line delineates the rupture extent and the black star identifies the epicenter.

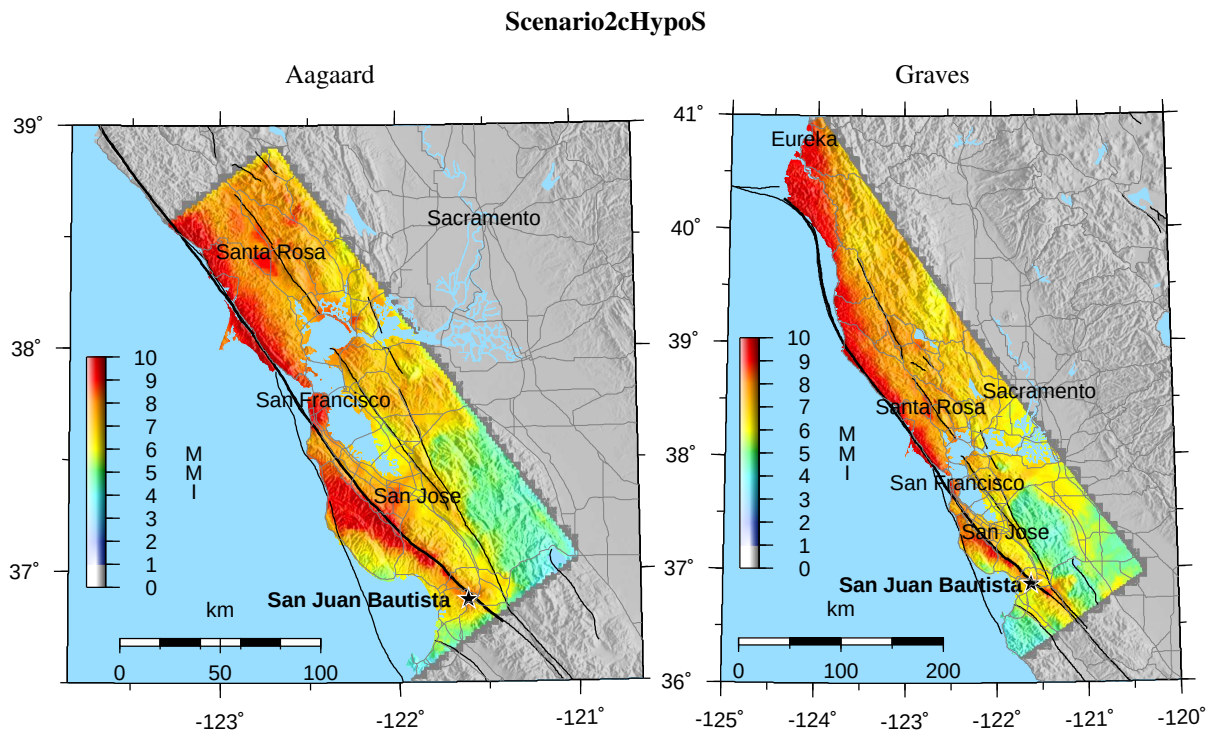

Figure 19. ShakeMaps for Aagaard's (T > 2.0 s, left) and Graves (T > 1.0 s, right) Scenario2cHypoS simulations. The thick black line delineates the rupture extent and the black star identifies the epicenter.

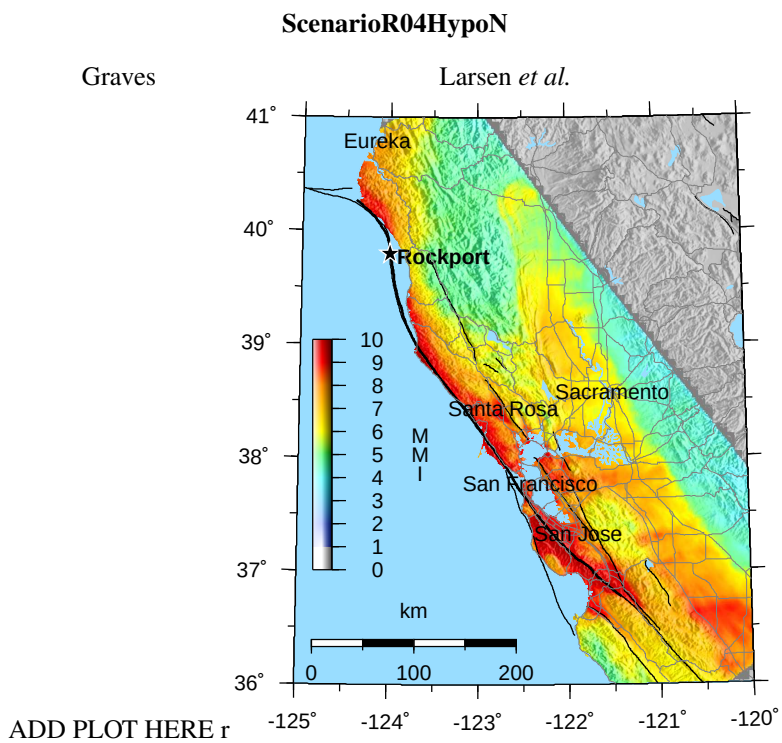

ADD PLOT HERE r

Figure 20. ShakeMaps for Graves's (T > 1.0 s, left) and Larsen *et al.*'s (T > 1.0 s, right) ScenarioR04HypoN simulations. The thick black line delineates the rupture extent and the black star identifies the epicenter.

ScenarioR04HypoC

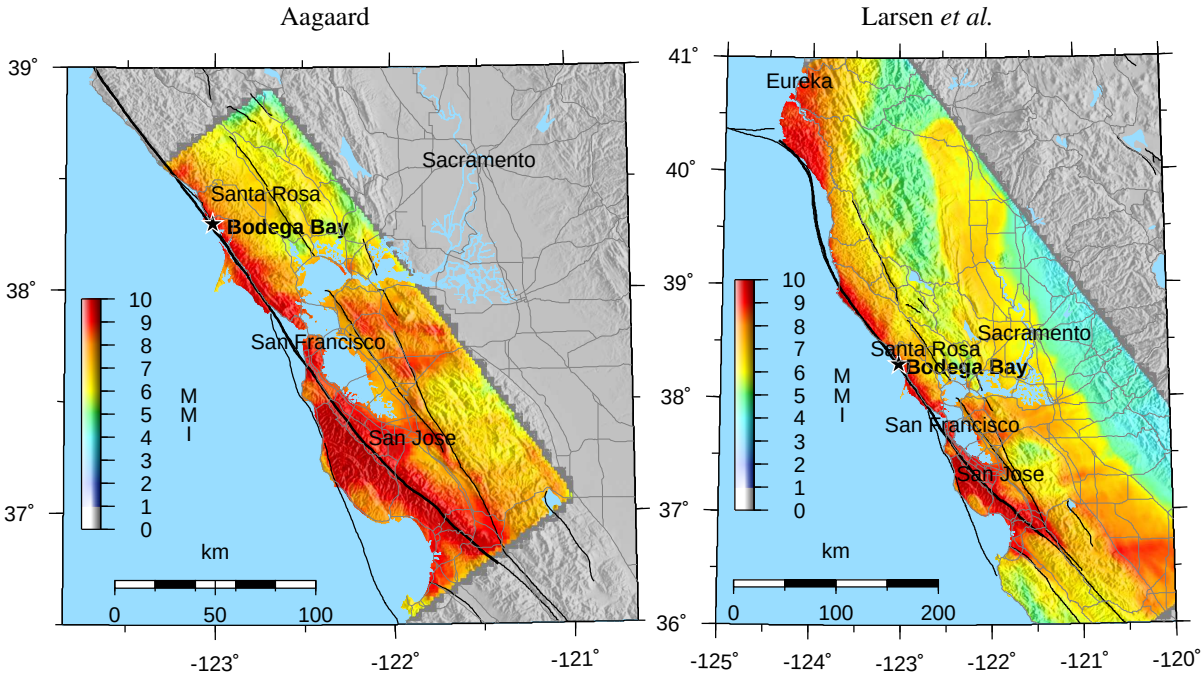

Figure 21. ShakeMaps for Aagaard's (T > 2.0 s, left) and Larsen *et al.*'s (T > 1.0 s, right) ScenarioR04HypoC simulations. The thick black line delineates the rupture extent and the black star identifies the epicenter.

ScenarioR04Hypo06

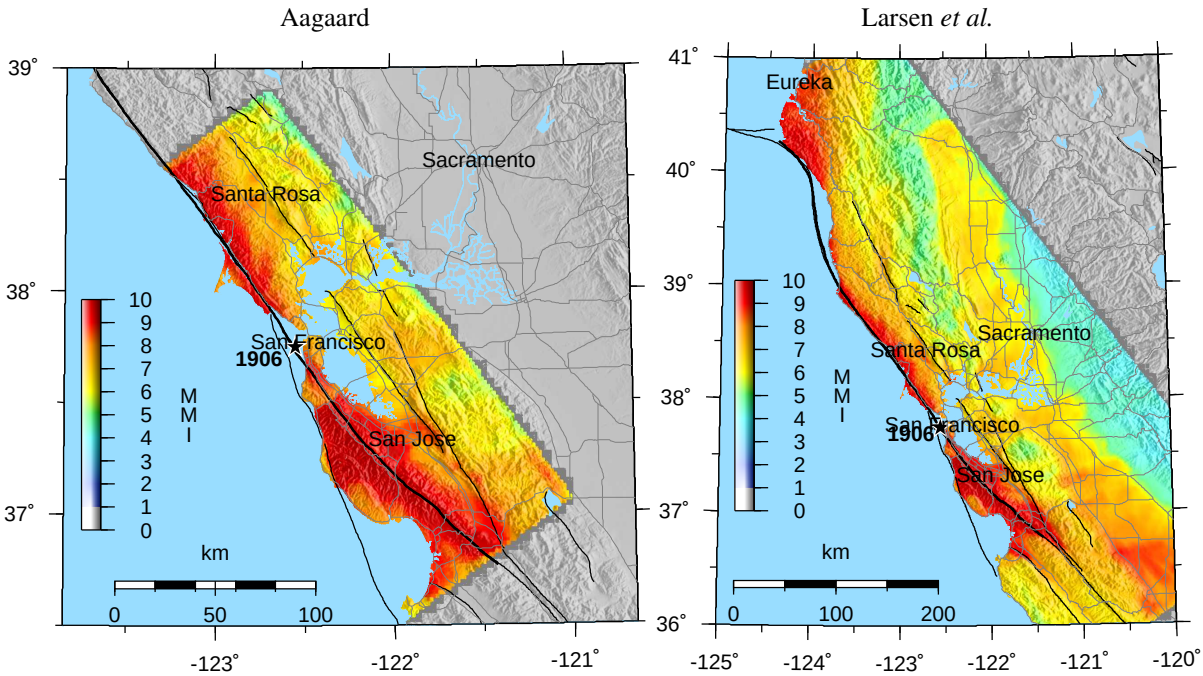

Figure 22. ShakeMaps for Aagaard's (T > 2.0 s, left) and Larsen *et al.*'s (T > 1.0 s, right) ScenarioR04Hypo06 simulations. The thick black line delineates the rupture extent and the black star identifies the epicenter.

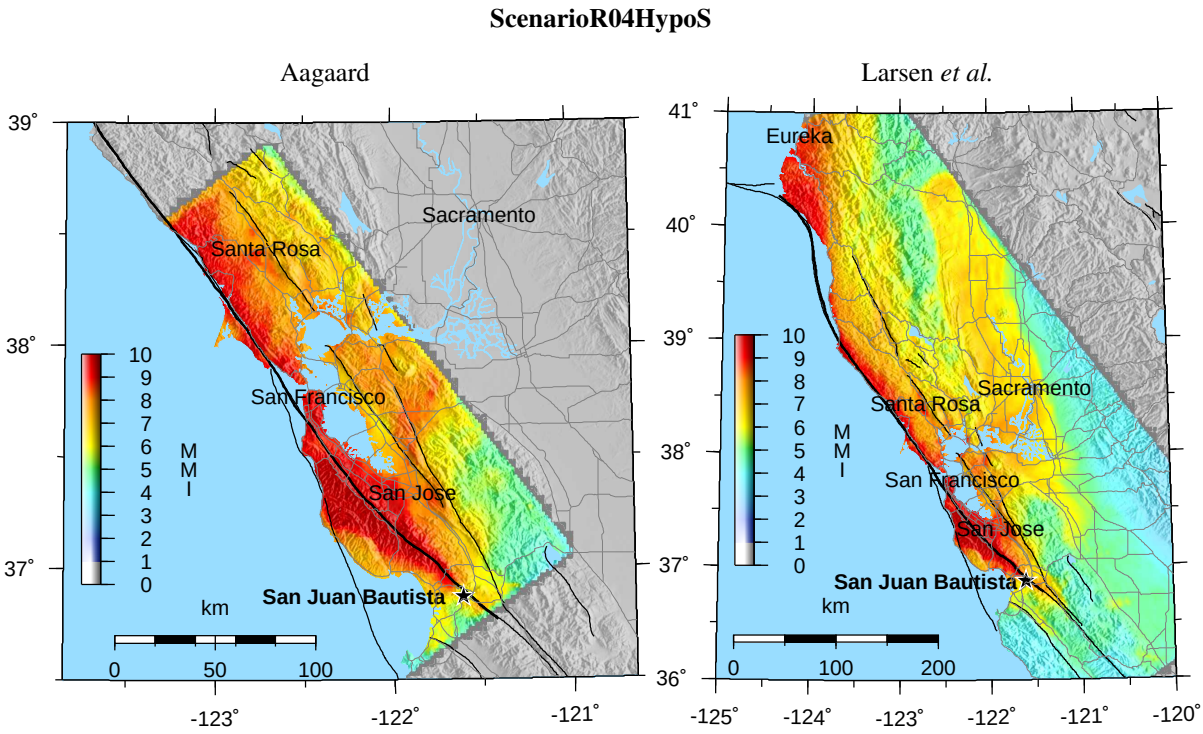

Figure 23. ShakeMaps for Aagaard's (T > 2.0 s, left) and Larsen *et al.*'s (T > 1.0 s, right) ScenarioR04HypoS simulations. The thick black line delineates the rupture extent and the black star identifies the epicenter.

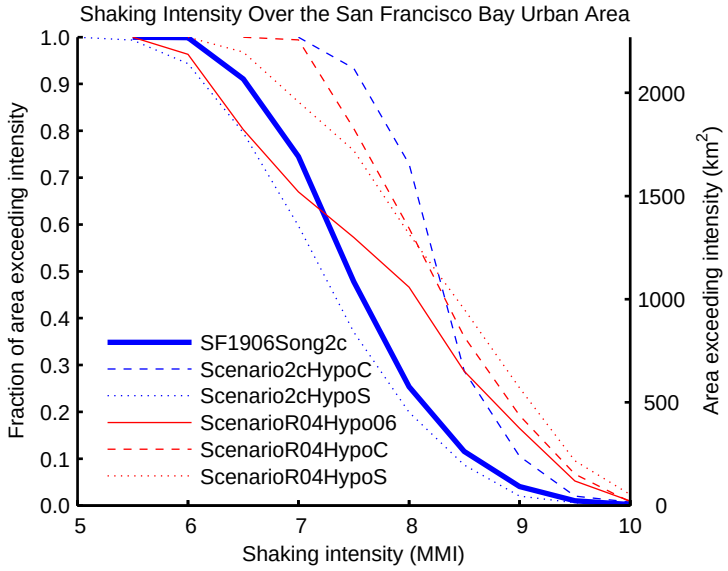

Figure 24. Comparison of fractions of the primary San Francisco Bay urban rea subjected to given levels of shaking intensity for Aagaard's simulations of the the 1906 earthquake (SF1906Song2c) and five hypothetical scenarios.